Reactive transport of CO_2-rich fluids in simulated wellbore interfaces: Flow-through experiments on the 1–6 m length scale

Timotheus K.T. Wolterbeek [a,*], Colin J. Peach [a], Amir Raoof [b], Christopher J. Spiers [a]

[a] HPT Laboratory, Faculty of Geosciences, Utrecht University, Budapestlaan 4, 3584CD Utrecht, The Netherlands
[b] Hydrogeology Group, Faculty of Geosciences, Utrecht University, Princetonplein 9, 3584CD Utrecht, The Netherlands

A B S T R A C T

Debonding at casing-cement interfaces poses a leakage pathway risk that may compromise well integrity in CO_2 storage systems. The present study addresses the effects of long-range, CO_2-induced, reactive transport on the conductance of such interfacial pathways. This is done by means of reactive flow-through experiments, performed on simulated wellbore systems consisting of cement-filled steel tubes, measuring 1.2–6.0 m in length. These were prepared by casting Class G HSR Portland cement into steel tubes (inner diameter 6–8 mm), followed by curing for 6–12 months. The tubes were subsequently pressurized to permanently inflate them off the cement, creating debonded cement-steel interfaces. Four experiments were performed, at temperatures of 60–80 °C, employing flow-through of CO_2-bearing fluid at mean pressures of 10–15 MPa, controlling the pressure difference at 0.12–4.8 MPa, while measuring flow-rate. The results show decreases in sample permeability of 2–4 orders, which microstructural observations reveal to be associated with downstream precipitation of calcium carbonates, possibly aided by migration of fines. This demonstrates that reactive-flow on the metre-scale significantly enhances the self-sealing potential of cement-casing interfaces relative to near-static reaction experiments. The results and method presented can be used not only to understand the long-range behaviour of annuli in wells qualitatively, but also to test reactive transport models which can then be applied at the field scale.

© 2016 Elsevier Ltd. All rights reserved.

1. Introduction

Wells are essential for providing access to geological formations considered for CO_2 storage, such as depleted oil and gas reservoirs or deep saline aquifers (Celia et al., 2009; Gasda et al., 2004; Hofstee et al., 2008; Whittaker et al., 2011). However, they inevitably penetrate the geological seal, posing a potential containment risk (Zhang and Bachu, 2011). Unwanted fluid migration must be minimized via the artificial barriers emplaced during well completion and abandonment, i.e. via the Portland-based cement seals usually injected into and around the steel casing. While these materials degrade if exposed to large volumes of CO_2-bearing fluid (Duguid and Scherer, 2010; Kutchko et al., 2007; Nešić, 2007), defect-free cement is generally considered to offer an adequate seal, because of its low matrix permeability (typically 10^{-22}–10^{-17} m^2, Montgomery, 2006; Taylor, 1992). This limits the extent of CO_2-induced reactions under the confined, restricted flow conditions expected at depth downhole (Bachu and Bennion, 2009; Carey, 2013; Duguid, 2009; Liteanu and Spiers, 2011).

However, as evidenced by numerous leaking natural gas wells (Bachu and Watson, 2006; Ingraffea et al., 2014; Jackson and Dusseault, 2014), the cement seals in old or inherited (legacy) wells cannot be assumed defect-free. Inadequate well completion or abandonment procedures (Barclay et al., 2001), curing-related cement shrinkage (Dusseault et al., 2000; Taylor, 1992) and operation-induced changes in wellbore temperature and/or stress-state (Lecampion et al., 2013; Mainguy et al., 2007; Orlic, 2009; Rutqvist, 2012; ter Heege et al., 2015) can lead to the formation of fractures in the cement or voids at the casing-cement and cement-formation interfaces. Such defects offer pathways for advective and reactive fluid transport. Under these conditions, CO_2-induced reactions are widely considered to pose an enhanced threat to well integrity (Carey, 2013; Deremble et al., 2011; Luquot et al., 2013; Zhang and Bachu, 2011).

Several studies have addressed the effects of CO_2-induced reactions on the transport properties of defect-bearing well materials, such as fractured cement (Abdoulghafour et al., 2013; Liteanu and Spiers, 2011; Luquot et al., 2013; Yalcinkaya et al., 2011), debonded cement-casing interfaces (Carey et al., 2010; Han et al., 2011;

Wolterbeek et al., 2013) and cement-rock interfaces (Jung et al., 2014; Mason et al., 2013; Newell and Carey, 2012; Walsh et al., 2014a; Wigand et al., 2009). In most of these studies, reaction experiments were performed on cylindrical samples measuring 1–10 cm in length, using either a batch reaction approach or maintaining a constant flow-through rate of CO_2-rich brine. While much insight has been gained from these experiments, the parameters that control whether reactive transport will be self-sealing or defect-enhancing remain poorly known. Particularly few data are available on the effects of two key factors.

The first concerns sample dimensions. Cement samples used in previous experiments have generally been too short to observe the effects of long-range geochemical gradients, though several studies have emphasized the importance of such gradients with respect to downstream mineral precipitation resulting from dissolution upstream (Armitage et al., 2013; Deremble et al., 2011). The second factor concerns boundary conditions. Most reactive flow-through tests employ a constant influx or flow-rate of CO_2-rich brine. By definition, doing so prevents the occurrence of self-limiting reactive-flow, precluding any transitions from advection-controlled to diffusion-controlled reactive-transport. These effects have only recently been addressed in experimental work, specifically by Cao et al. (2015) and Huerta et al. (2016), who employed composite cement samples up to ~30 cm in length and imposed a constant differential pressure. However, noting the length scale of real wells and the likely hydrodynamic conditions, these two factors are still insufficiently explored to understand and model the evolution of wellbore integrity confidently. In particular, data are needed on the effects of long-range reactive transport on debonding defects at the casing-cement interface. Previous work on these defects under (near-)static reaction conditions suggests that they have very limited sealing-potential, due to the formation of passivating corrosion scale films on both steel and cement (Wolterbeek et al., 2013). Against this background, the present study addresses the effects of reaction with supercritical CO_2-rich fluid on the transport properties of interconnected defects along 1–6 m sections of simulated cement-casing interface. This is done by means of reactive flow-through experiments on coiled, cement-filled steel tubes, with debonded interfaces, employing a controlled fluid pressure difference across the sample to allow for self-limiting reactive-flow. The experiments were performed at temperatures of 60 and 80 °C, at mean fluid pressures of 10–15 MPa, i.e. approaching downhole conditions. Our results demonstrate that reactive-transport on the 1–6 m scale contributes significantly to the self-sealing potential of defects in wells. They also provide new insight into the processes that govern transport through annuli in wells on length scales well beyond those employed in laboratory experiments to date.

2. Experimental methods

2.1. Sample materials and preparation

Metre-scale sections of debonded wellbore casing-cement interface were simulated using coiled steel tubes filled with cement. These were prepared as follows. First, lengths measuring 1.2–6.0 m were cut from ST.35 type steel tubing (EN 10305-3, wall thickness 1 mm) and fitted with Nova high-pressure line connectors. Cement slurry was then prepared from API-ISO Class G HSR Portland clinker (Dyckerhoff AG, Lengerich) using deionised water at a water-to-cement ratio of 0.44, in accordance with ISO standards 10426-1 and 10426-2 (API Specification 10A, Recommended Practice 10B-2). The cement slurry was subsequently injected into the steel tubes using a peristaltic pump, the tube ends were sealed

and the cement was allowed to cure. For each sample, a duplicate section of cement-filled steel tube (~20 cm long) was prepared as a reference system for TGA and XRD analysis.

Four coiled samples were fabricated (Table 1), using three slightly different procedures to achieve coiling:

1) In the case of samples T60-1 and T60-2, the cement slurry was injected into a straight steel tube (inner diameter 6 mm, length 6.0 m) and cured at room temperature (RT) for a period of >6 months, while in a vertical orientation. After curing, the tubes were bent into a coil (diameter ~23 cm, pitch ~1 cm). This process induced (disc) cracks in the cement.
2) Sample T80-1 was prepared similarly, but using a tube of 2.0 m length and 8 mm inner diameter (ID). In this case, the cement was allowed to cure at RT for 12 months, after which the tube was bent into a coil of ~15 cm diameter (pitch ~1 cm).
3) In the case of sample T80-2, the cement slurry was injected into a pre-coiled steel tube (~15 cm coil diameter, pitch ~1 cm, tube ID 6 mm, length 1.2 m), which was cured in a thermobath at 80 °C for 12 months, with the windings orientated horizontally.

After curing, the Nova high-pressure connectors plus tube ends (~3 cm) of all four samples were drilled out to remove the hardened cement. This was done to avoid clogging of the connectors and to ensure uniform application of fluid pressure to the ends of the main cemented section of the coiled sample.

One end of each coil was then connected to a high pressure hand-spindle pump while the other was fitted with a pressure gauge and sealed. Debonding at the steel-cement interface was achieved by injecting water into one end using the pump, increasing the pressure stepwise to 100–130 MPa. This caused the wall of the steel tube to permanently deform and lift-off of the cement. This procedure was executed slowly, over 3–4 weeks, to obtain uniform expansion of the steel tube. The size of the aperture imposed was monitored throughout by measuring the outer diameter of the tube, using a micrometer screw gauge. Sample T80-2 was not debonded hydraulically, due to substantial initial permeability.

2.2. Reactive flow-through apparatus

2.2.1. Permeameter

Our reactive flow-through experiments were performed in a purpose-built permeameter system (Fig. 1), capable of running at temperatures up to 80 °C (±0.5 °C) and fluid pressures of 10–15 MPa, thus approaching downhole well conditions. The main setup consisted of two temperature-controlled Teledyne ISCO syringe pumps (models 500D and 65D for the 60 °C and 80 °C experiments, respectively), connected to the up- and downstream ends of the cemented-filled steel-coil sample (Fig. 1a). The pumps, controlled using LabView-based software, were operated in constant pressure mode, together maintaining a constant pressure difference (0.12–4.8 MPa) across the sample. Both pumps were equipped with Honeywell Model TJE pressure transducers (resolution ~10 kPa), as well as demineralised water and vacuum connections. The upstream (US) pump was also connected to a reactor vessel system (Fig. 1b), used to pre-equilibrate and source the CO_2-bearing aqueous phase constituting the inlet fluid. During the experiments conducted at 60 °C, a Keller PD-33X/80990 differential pressure transducer (resolution ~1 kPa), mounted between the syringe pumps, was used to corroborate the syringe pump pressure data. In all experiments, the coiled sample was immersed in a silicone oil thermobath, used to circulate heated fluid through temperature control jackets on the two pumps, thus maintaining these components at experimental temperature. The high pressure tubing connecting the remaining components of the setup was heated

Table 1
Summary of sample characteristics, experimental conditions and key data.

configuration | conditions | data	experiment/sample code			
	T60-1	T60-2	T80-1	T80-2
steel tube length (L) [m]	6.0	6.0	2.0	1.2
steel tube inner diameter ($2R_{tube}$) [mm]	6.0	6.0	8.0	6.0
Temperature (T) [°C]	60	60	80	80
initial pressure difference (ΔP) [MPa]	~0.6	~0.6	~0.2	~0.12
initial fluid flux (Q_{LRC}) [ml h^{-1}]	7.2	68.6	3.7	7.9
assumed fluid viscosity at test P-T (μ) [Pa s]	4.84×10^{-4}	4.84×10^{-4}	3.69×10^{-4}	3.69×10^{-4}
initial sample permeability (κ_{LRC}) [m^2]	3.4×0^{-13}	3.3×10^{-12}	1.0×10^{-13}	3.0×10^{-13}
final sample permeability (κ_{LRC}) [m^2]	2.9×10^{-17}	6.0×10^{-15}	8.2×10^{-18}	6.9×10^{-16}
initial hydraulic aperture[a] (w_{hydr}) [μm]	18.3	39.0	12.0	17.3
observed defect type[b]	debonded annulus	debonded annulus	debonded annulus	crescent-shaped interfacial void
observed defect aperture[b] (w_{obs}) [μm]	~60	~200	~20	~150
downstream extent of Zone II[b] [cm]	50–70	180–230	15–25	>120?
downstream extent of alteration[c] [cm]	73	230	17	>120

[a] Calculated from the initial sample permeability, assuming that the interfacial defect can be represented by an annular region between two concentric cylinders – see Section 4.3 and model Bird et al. (2002).
[b] Estimated from microstructural observations (Figs. 3–7).
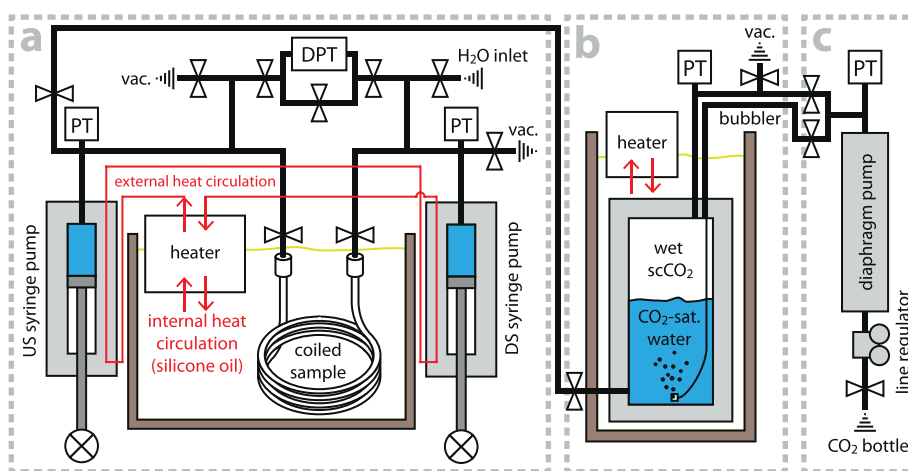[c] Determined from TGA data (Fig. 9).

Fig. 1. Schematic diagram of the reactive flow-through permeameter setup. US = upstream, DS = downstream, PT = pressure transducer, vac. = vacuum port. (a) Constant pressure-difference permeameter, plus the coiled sample; (b) CO_2-H_2O pre-mixing vessel; (c) CO_2 pressure system. Note that components (a) and (b) were maintained at test temperature during individual experiments.

electrically using insulated heating tape. The thermobath and heating tape temperature were controlled at test temperature to within 0.1 °C. All non-immersed parts were insulated using fibreglass and Styrofoam. The functionality of the permeameter was tested during benchmark experiments (described in Appendix A).

2.2.2. CO_2-H_2O fluid source system

The CO_2-bearing aqueous phase used in the reactive flow-through experiments was prepared in the mixing vessel shown in Fig. 1b (volume ~1.2 l). This was maintained at either 60 or 80 °C (±0.5 °C), in accordance with the intended flow-through conditions. The vessel was equipped with a Keller PAA-33X pressure transducer, a vacuum connection and two CO_2 inlets (one, with a bubbler to promote mixing) at the top, and a connection to the US pump at the bottom of the vessel (Fig. 1b). Prior to each experiment, the mixing vessel was 75%-filled with demineralised water, evacuated to remove air and pressurised with CO_2 using a Sprague S216J60 EPR diaphragm pump (Fig. 1c). Per experiment, the supercritical CO_2 plus H_2O mixture was allowed to equilibrate at temperature for about a week, maintaining the pressure inside the reaction vessel at 9.5 MPa. This fluid was estimated to have a pH of ~3.2 at 60–80 °C and 10 MPa pressure, using the model by Duan and Sun (2003).

2.3. Reactive flow-through testing procedure

The reactive flow-through experiments generally involved an initial reference permeability measurement, performed using demineralised water, followed by introduction of supercritical CO_2-rich water. To make the initial reference determination, each coiled sample was mounted in the permeameter and the two syringe pumps plus sample were charged with deaerated, demineralised water by vacuum-flushing. The pump-sample system (Fig. 1a) was then pressurized to 10 MPa and, after initial calibrations and leak tests, brought to experimental temperature and allowed to equilibrate for ~10 h. Subsequently, the US and DS pumps were isolated from the sample and the upstream pressure was increased to the desired value (10.12–10.6 MPa). Quantitative leak-rate calibrations were performed (duration >24 h) on the individual, isolated pumps at this stage. The sample and DS pump were then connected and allowed to fully (re)equilibrate at a downstream pressure of 10 MPa over ~10 h, prior to permeability measurement.

The reference flow-through experiment using water was initiated by opening the connection between the US pump and the sample, thereby imposing a constant fluid pressure difference across the sample. The magnitude of the resulting flow from the US to DS pump provides a measure of initial (apparent) sample permeability. Note that where required to obtain a stable initial

permeability with respect to water, the samples were flushed to remove fines created during the debonding process, then making the reference measurement.

The switch from flow-through of water to CO_2-bearing fluid was initiated when the US pump was emptied of water. The US pump was then isolated from the sample, connected to the reaction vessel (Fig. 1b) and filled with CO_2-saturated water in flow-rate control mode. During this procedure, the pressure of 9.5 MPa in the reaction vessel (and hence in the US syringe pump) was maintained nominally constant by supplying CO_2 using the Sprague diaphragm pump (Fig. 1c). The water-filled DS pump and sample were maintained at 10 MPa. Once filled with CO_2-saturated aqueous fluid at reaction vessel P-T conditions, the US syringe pump was isolated from the reaction vessel and pressurized further to the desired upstream pressure (10.12–10.6 MPa), in pressure control mode. Flow was then initiated through the sample into the DS pump with the DS pressure held at 10 MPa. Under these conditions, the amount of CO_2 dissolved in the aqueous fluid captured in the US pump (at 10.12–10.6 MPa) equals the equilibrium concentration in the reaction vessel at 9.5 MPa and test temperature, which is slightly lower than the equilibrium CO_2 concentration at the pressure of 10 MPa in the DS pump. While this approach leaves the fluid undersaturated with respect to CO_2 at the US and DS pump pressures, it inhibits CO_2 degassing during flow, which might otherwise yield multiphase flow effects. Permeability measurement was continued for a total of 250–870 h, intermittently suspending measurement by isolating the sample to re-stroke and/or recharge the pumps. After such events, the sample-pump system was allowed to settle for about one hour, before permeability measurement was continued by reconnecting the sample.

2.4. Data acquisition and processing

2.4.1. General aspects

A PC equipped with LabView-based software was used to log the pump volume, flow-rate, pressure and differential pressure signals every 2 s throughout the flow-through runs. The data obtained were processed by removing data intervals corresponding to pump re-stroking or other maintenance, correcting for both volume and time offsets accordingly. All data records were then smoothed by averaging over two-minute intervals. As already indicated, individual pump leak-rates were obtained from calibrations performed before (and after) each experiment. Whole system leakage during our experiments was estimated using total volume data (i.e. the sum of US and DS pump volume data versus time), ignoring small changes in total volume due to chemical reaction (Matschei and Glasser, 2007).

Assuming single-phase flow, the processed data were used to calculate the evolution of the apparent Darcy permeability of each coiled sample [m²], defining this here as (e.g. Guéguen and Palciauskas, 1994).

$$\kappa_{app} = \mu \frac{Q_S}{A} \frac{L}{\Delta P} \tag{1}$$

where μ is the dynamic viscosity of the fluid [Pa s], Q_S is the fluid flux traversing the sample [m³ s⁻¹], L and A are the length [m] and cross-sectional area [m²] of the coiled sample, respectively, and ΔP is the pressure difference across the sample, i.e. that measured between the US and DS pumps [Pa]. Q_S was obtained at specific times by smoothing pump volume versus time data using a moving average method, followed by linear regression over intervals up to two hours. Corresponding values for ΔP, leak-rates and pump volumes versus time were obtained using the same moving average method.

2.4.2. Accounting for uncertainty due to leaks

The fluid fluxes obtained from the measured pump volume data inevitably contain contributions from minor leaks, resulting in systematic error. Specifically, the fluid flux estimate obtained from US pump data (Q_{pump}^{US}) represents the fluid flux through the sample (Q_S) plus the flux lost via any leaks in the permeameter upstream of the sample (Q_{leaks}^{US}) so that $|Q_{pump}^{US}| = |Q_S| + |Q_{leaks}^{US}|$. Similarly, for the DS pump $|Q_{pump}^{DS}| = |Q_S| - |Q_{leaks}^{DS}|$. We defined minimum and maximum bounds for apparent sample permeability [m²], based on DS and US pump volume data, as

$$\kappa_{\min} = \mu \frac{|Q_{pump}^{DS}|}{A} \frac{L}{\Delta P}$$
$$\kappa_{\max} = \mu \frac{|Q_{pump}^{US}|}{A} \frac{L}{\Delta P} \tag{2}$$

If leakage is negligible compared to the flux through the sample (Q_S), then $\kappa_{\min} \approx \kappa_{\max} \approx \kappa_{app}$. However, if leakage contributes substantially to Q_{pump}^{DS} or Q_{pump}^{US}, then $\kappa_{\min}$ and $\kappa_{\max}$ will reflect the associated uncertainty in κ_{app}. To obtain a best estimate for κ_{app}, we corrected for leaks as follows. Using the leak-rates $Q_{isolated}^{US}$ and $Q_{isolated}^{DS}$ obtained in calibrations before and after each reactive flow-through experiment, the fraction of the system leak-rate attributable to leakage upstream of the sample was quantified as

$$f_{US} = \frac{|Q_{isolated}^{US}|}{|Q_{isolated}^{US}| + |Q_{isolated}^{DS}|} \tag{3}$$

Assuming f_{US} does not change significantly upon initiation of flow-through, this fraction was used to define a leak-rate-corrected (LRC) apparent sample permeability [m²] given

$$\kappa_{LRC} = \mu \frac{|Q_{pump}^{US}| - f_{US} Q_{leak}^{TOTAL}}{A} \frac{L}{\Delta P}$$
$$= \mu \frac{|Q_{pump}^{DS}| + (1 - f_{US}) Q_{leak}^{TOTAL}}{A} \frac{L}{\Delta P} \tag{4}$$

Here $Q_{leak}^{TOTAL} = |Q_{leak}^{US}| + |Q_{leak}^{DS}| = |Q_{pump}^{US}| - |Q_{pump}^{DS}|$ was determined by linear regression applied to the whole system volume versus time data, i.e. neglecting reaction-induced changes in whole system fluid volume.

Henceforth, in presenting our apparent permeability results we use κ_{LRC}, which provides a best approximation for the apparent sample permeability, adding $\kappa_{\min}$ and $\kappa_{\max}$ to specify the associated uncertainty limits.

2.4.3. Accounting for other errors

Errors due to other sources were estimated assuming that these could be regarded as independent and random. Neglecting small errors in L and A, and those resulting from temperature variations, the net error in κ_{app}, as given by Eq. (1), is

$$\frac{\delta \kappa_{app}}{\kappa_{app}} \approx \sqrt{\left(\frac{\delta \mu}{\mu}\right)^2 + \left(\frac{\delta \Delta P}{\Delta P}\right)^2} \tag{5}$$

where the prefix δ refers to the error or uncertainty in the associated quantity (cf. Taylor, 1997). Equivalent expressions apply for Eqs. (2) and (4).

Let us focus first on $\delta \mu$. The dynamic viscosity, μ [Pa s], of an aqueous fluid depends on its temperature, salinity and dissolved CO_2 content (Fleury and Deschamps, 2008; Islam and Carlson, 2012; Mao and Duan, 2009). In our experiments, fluid composition, hence μ, cannot be constrained accurately, given the complex chemical reactions involved. In calculating apparent sample permeability using Eqs. (2) and (4), we therefore assumed a constant μ-value of either 4.84×10^{-4} Pa s (at 60 °C) or 3.69×10^{-4} Pa s (at

80 °C), corresponding to the dynamic viscosity of a 0.3 M NaCl solution at 10 MPa fluid pressure and the said temperatures (following Mao and Duan, 2009). A salinity of 0.3 M NaCl was chosen to reflect the ionic strength of a typical cement pore fluid (Andersson et al., 1989; Rothstein et al., 2002). We neglected any effects of reaction-induced changes in ionic species entering/leaving the solution or in dissolved CO_2 content. If true salinity fell in the range 0–1 M in our experiments, use of our fixed reference value of 0.3 M would introduce relative errors in dynamic viscosity ($\delta\mu/\mu$) of up to $\pm10\%$ (Mao and Duan, 2009). Neglecting dissolved CO_2 content may yield relative errors of a similar magnitude at high ionic strength (Islam and Carlson, 2012). Turning now to $\delta\Delta P$ in Eq. (5), this was estimated to be ~0.02 MPa, from permeameter calibrations, implying a relative error ($\delta\Delta P/\Delta P$) of $\leq15\%$ compared to the pressure differences of 0.12–4.8 MPa applied during the experiments. On this basis, the net relative uncertainty in κ_{min}, κ_{max} and κ_{LRC} due to random errors was estimated to be at most 30%.

2.5. Post-experiment microstructural and mineralogical analysis

After completion of the reactive flow-through experiments, the four coiled samples were subjected to mineralogical and microstructural study. To this end, the samples were first dried in an oven at 60 °C for 48 h, then cut into lengths of approximately 2.5 cm. Cross-sections measuring 2 mm in thickness were then cut, from the middle of selected lengths, to obtain a sequence (from inlet to outlet) of sections oriented normal to the flow direction. These were studied using reflected light microscopy and micro-X-ray fluorescence analysis (μXRF), followed by scanning electron microscopy plus energy-dispersive X-ray spectroscopy (SEM-EDX). The sections were Pt/Pd-coated for the latter, allowing carbonates and hydroxides/oxides to be discerned. The cementitious contents of the remaining lengths of tube were removed and crushed into a powder, to be used in X-ray diffraction (XRD) and thermogravimetric (TGA) analysis. Reference data for TGA and XRD were obtained from crushed cement obtained from ~2.5 cm lengths, cut midway from the 20 cm long reference samples. The reference samples were not used for microstructural analysis, as they did not experience hydraulic debonding.

TGA analysis was performed on the powdered contents of the segments by increasing the temperature from RT to 900 °C, at a rate of $10\,^\circ$C min^{-1} (cf. methods in Lothenbach et al., 2007; Luquot et al., 2013; Taylor, 1992). Weight loss during heating, which occurs as H_2O and CO_2 are released by thermal decomposition, allowed the portlandite and calcium carbonate content of the reacted cement material to be estimated. Following Taylor (1992), results were referred to the ignited weight, since the initial weight will have included a relatively arbitrary amount of free and loosely bound water.

3. Results

Key data obtained in the four reactive flow-through experiments performed are summarized in Table 1. In the following, we first describe the flow-through permeametry results, followed by detailed microstructural, (micro)chemical and mineralogical observations.

3.1. Apparent permeability evolution

Given the low matrix permeability of cement (typically 10^{-21}–10^{-17} m^2, cf. Montgomery, 2006; Taylor, 1992), flow in the coiled samples presumably occurred predominantly via annuli at the cement-steel interface created during sample preparation. However, the exact defect geometry and its evolution during the experiments are unknown, since microstructural analysis could

only be performed after test completion. We accordingly present the evolving transport properties of the coiled samples in terms of the apparent sample permeability, expressed as κ_{LRC} [m^2] (plus κ_{min} and κ_{max}), calculated with respect to the initial internal cross-sectional area of the steel tubes, using factory tube dimensions. Therefore, the data presented here include the effects of both chemical reaction and minor changes in defect dimensions due to variation in fluid pressure.

3.1.1. Sample T60-1

The apparent permeability, κ_{LRC}, of coiled sample T60-1 (ID 6 mm, length 6 m) remained constant at ~3.4×10^{-13} m^2 during 4 h of initial water-based measurement at $\Delta P = 0.6$ MPa (Fig. 2a,b). After introduction of CO_2-bearing fluid, holding ΔP constant, the permeability decreased by nearly two orders, to ~7.6×10^{-15} m^2, over ~57 h. Due to a power failure, the test was then interrupted for ~30 h, during which time the permeameter system had to be restarted and recalibrated for leaks. Upon reinitiation (at $t = 87$ h), the apparent sample permeability continued to decrease at a similar rate, reaching $\kappa_{LRC} \approx 1.3\times10^{-15}$ m^2 after 109 h. At this point, the pressure difference was increased to $\Delta P = 1.8$ MPa using the US pump, to reduce the significance of leaks in the US pump (Fig. 2a,b). Following this step, the apparent sample permeability continued to decrease, though at a progressively decelerating rate, reaching $\kappa_{LRC} \approx 2.8\times10^{-16}$ m^2 at 258 h (Fig. 2a). The pressure difference was then increased to $\Delta P = 4.8$ MPa. This produced a direct increase in apparent permeability. The apparent sample permeability returned to pre-pressure step values within 48 h, however, and continued to decrease until shortly before termination of the experiment at 877 h, when κ_{LRC} approached ~2.9×10^{-17} m^2, effectively the lower measurement limit for this sample length. In total, ~25 ml of water and ~90 ml of CO_2-bearing fluid were injected during experiment T60-1.

3.1.2. Sample T60-2

The initial water permeability of sample T60-2 (ID 6 mm, length 6 m) was ~3.3×10^{-12} m^2, about an order higher than that of T60-1 (Fig. 2c,d). This remained constant during 7 h of water injection (~460 ml) at $\Delta P = 0.6$ MPa. Upon introduction of CO_2-bearing fluid at the same ΔP, the apparent sample permeability dropped rapidly, attaining a near-stable value of $\kappa_{LRC} \approx 9.3\times10^{-15}$ m^2 after 41 h (~100 ml injected of CO_2-bearing fluid). Increasing ΔP to 1.8 MPa had little effect (see Fig. 2d, range 100–200 ml). Increasing ΔP to 4.8 MPa resulted in slow fluctuations, with permeability first decreasing by about 30% and then increasing back to ~8.0×10^{-15} m^2, after which a slowly decreasing trend was once again established (Fig. 2c,d). Decreasing ΔP back to 1.8 MPa resulted in a small, instantaneous reduction in apparent permeability, κ_{LRC}, which subsequently remained more or less constant at ~6.0×10^{-15} m^2. In total, this experiment involved the flow-through of ~350 ml of CO_2-bearing fluid.

3.1.3. Sample T80-1

The initial apparent water permeability, κ_{LRC}, of coil T80-1 (ID 8 mm, length 2 m), measured at $\Delta P = 0.2$ MPa, was ~1.0×10^{-13} m^2. This remained constant during 12 h of flow-through using water, injecting ~41 ml (Fig. 2e,f). Introduction of CO_2-bearing fluid at $\Delta P = 0.2$ MPa, once again resulted in a rapid decrease in apparent sample permeability, which dropped about three orders before attaining a more or less stable value of $\kappa_{LRC} \approx 8.0\times10^{-17}$ m^2 after 90 h. At 180 h, ΔP was increased to 2 MPa, producing a transient increase in permeability. This lasted for about a day, after which the permeability gradually decreased to a value of $\kappa_{LRC} \approx 8.2\times10^{-18}$ m^2 (the lower measurement limit at $\Delta P = 2$ MPa), shortly prior to experiment termination. In total, ~30 ml of CO_2-rich fluid was injected (Fig. 2f). The experiment was terminated by per-
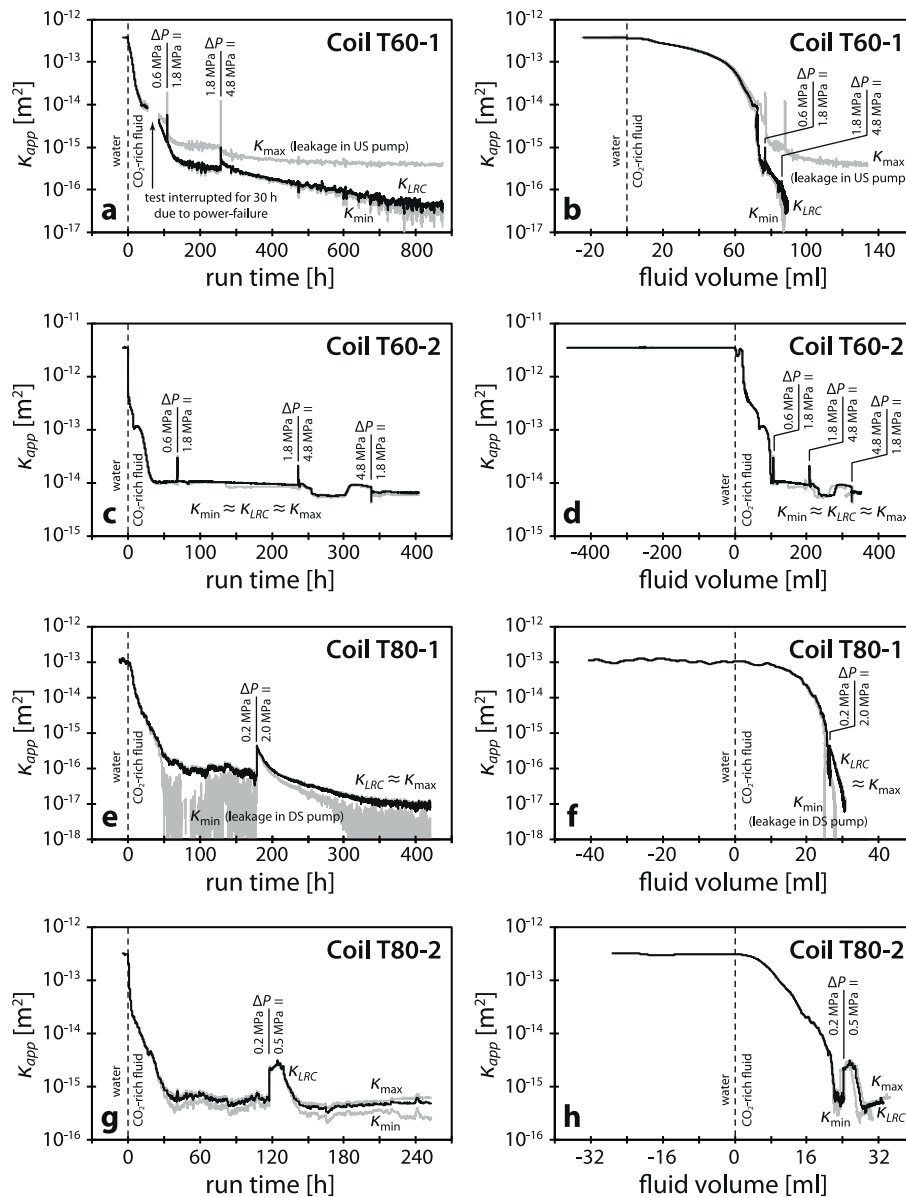
Fig. 2. Apparent sample permeability (κ_{app}), expressed in terms of κ_{min}, κ_{max} and κ_{LRC}, versus elapsed run time and injected fluid volume, for coiled samples T60-1 (a–b), T60-2 (c–d), T80-1 (e–f) and T80-2 (g–h). Zero run time and zero injected volume are taken at the moment flow-through using CO_2-bearing aqueous fluid was started. Our, water-based permeametry results are therefore plotted in the negative time and volume domains.

forming a final series of transient step permeametry tests (Hsieh et al., 1981; Neuzil et al., 1981) for control purposes. This yielded a permeability of $\sim 8.4 \times 10^{-18}$ m² (not plotted in Fig. 2e,f).

3.1.4. Sample T80-2

Coil T80-2 (ID 6 mm, length 1.2 m) also showed a stable, though relatively high initial sample permeability with respect to water of $\sim 3.0 \times 10^{-13}$ m². This was measured using $\Delta P \approx 0.12$ MPa (Fig. 2g,h). After injection of ~ 27 ml of water, CO_2-bearing fluid was introduced, also at $\Delta P \approx 0.12$ MPa. The permeability initially decreased similarly to T80-1. In T80-2, however, a more or less constant permeability of $\kappa_{LRC} \approx 5.6 \times 0^{-16}$ m² was reached after only 45 h (cf. Fig. 2g and e). Upon increasing ΔP to 0.5 MPa, a transient increase was again observed, decaying to a minimum in permeability of $\kappa_{LRC} \approx 5.7 \times 10^{-16}$ m², occurring some 30 h later. The apparent permeability then increased slowly, reaching $\kappa_{LRC} \approx 6.9 \times 10^{-16}$ m² at about 250 h of run time (~ 31 ml of CO_2-bearing fluid injected), at which point severe leakage forced termination of the experi-

ment. Note that the volume of CO_2-bearing fluid injected during the period of initial permeability decrease, was approximately 20–25 ml in both T80-2 and T80-1.

3.2. Microstructural and mineralogical observations

Upon removal from the permeameter setup, the cement inside each of the coil samples was visibly wet, orange-brown in colour at the inlet side (i.e. the upstream end of the cement) and grey at the downstream end. The inside of the steel tube, as far as free of cement and visible, was coated by a thin corrosion scale film.

3.2.1. Reflected light and scanning electron microscopy

Sections cut normal to the tube axis, hence flow direction, revealed the post-experiment defect geometries of all four coiled samples, as well as alteration and chemical zonation in the cement. Figs. 3–5 show reflected light images of progressively more distal cross-sections through the four samples. The downstream
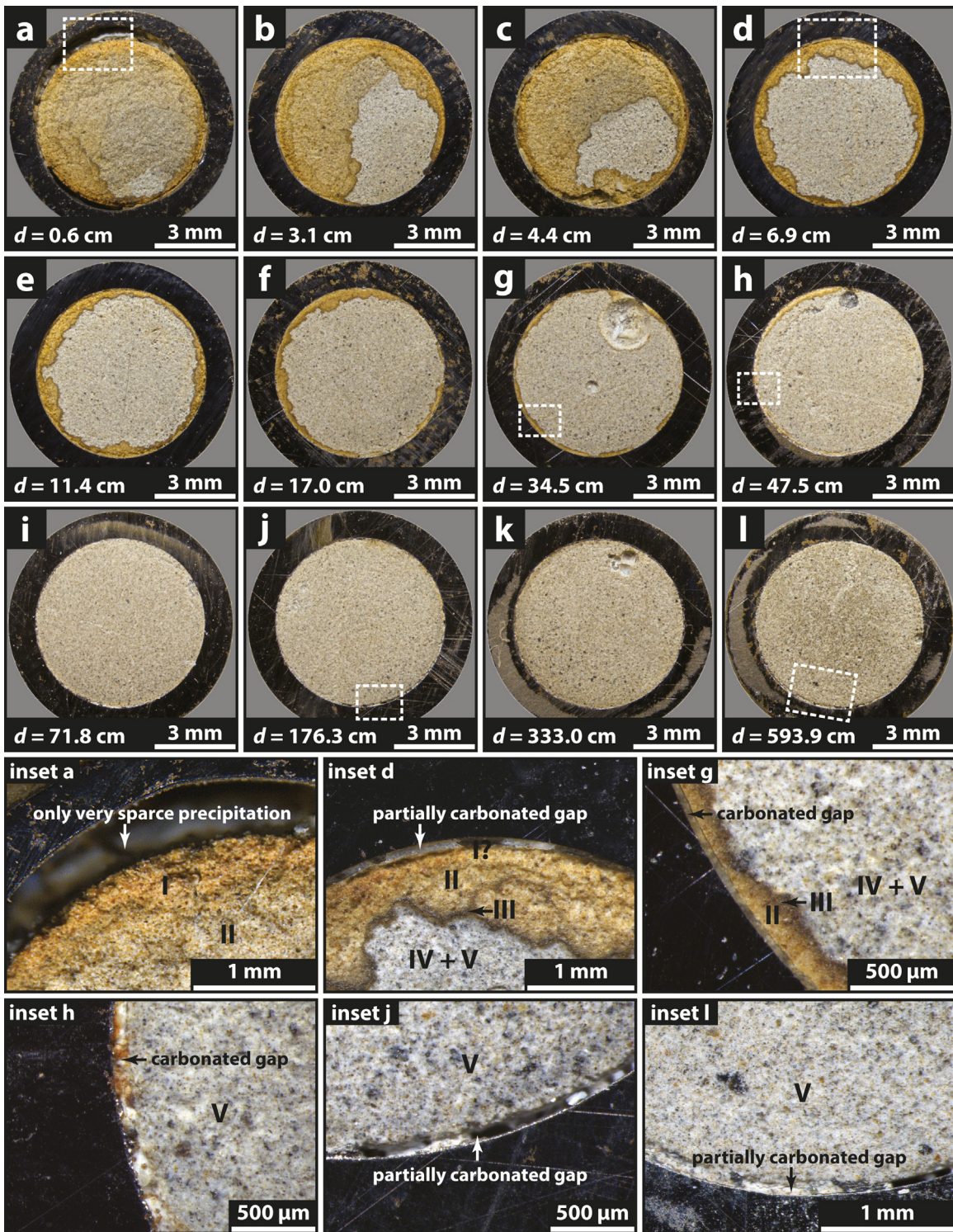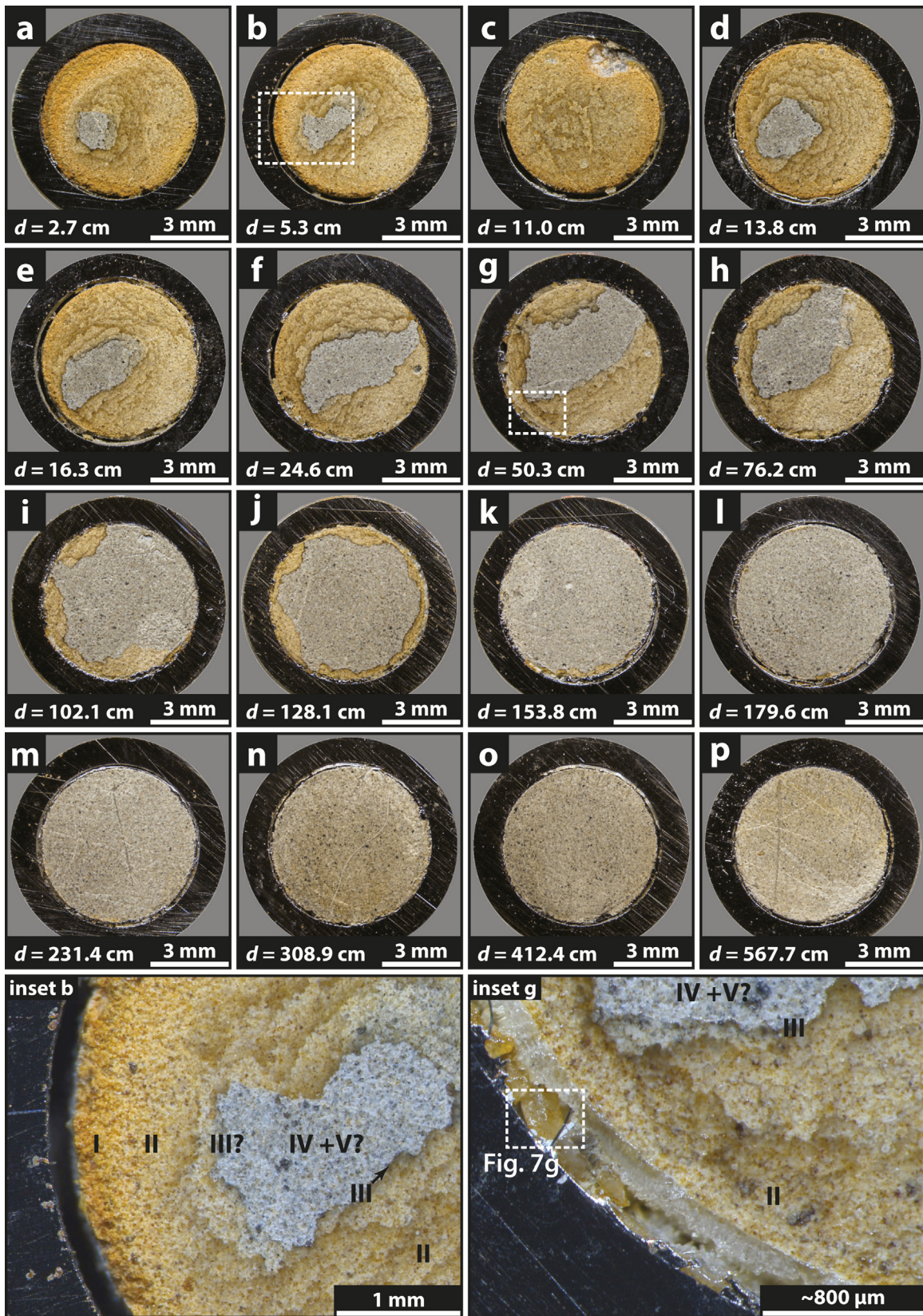
Fig. 3. Reflected light photographs of successively more distant cross-sections through coiled sample T60-1. Distance d [cm] from the upstream inlet is indicated for each section. Azimuthal orientation of cross-sections is roughly constant.

positions of these cross-sections are indicated schematically in Fig. 6, together with a simplified graphical representation of the features described in the three subsections below. Fig. 7 shows scanning electron micrographs of specific features in all four samples. Note that the azimuthal orientation of the cross-sections differs between images obtained via the different techniques.

3.2.1.1. Defect geometry. Sample T60-1 (Fig. 3) was characterized by a nearly radially symmetric, annular debonding defect at the cement-steel interface (Fig. 3a,d + insets). Short-ranged, shallow fractures, apparently orientated subparallel to the section plane and presumably formed as the hardened cement-filled steel tube was bent into a coil shape, were occasionally observed in the bulk cement. Within 2 cm of the inlet, the annulus attained large apertures up to ∼700 μm wide (Fig. 3a). These large apertures were

Fig. 4. Reflected light photographs of successively more distant cross-sections through coiled sample T60-2. Distance *d* [cm] from the upstream inlet is indicated for each section. Azimuthal orientation of cross-sections is roughly constant.
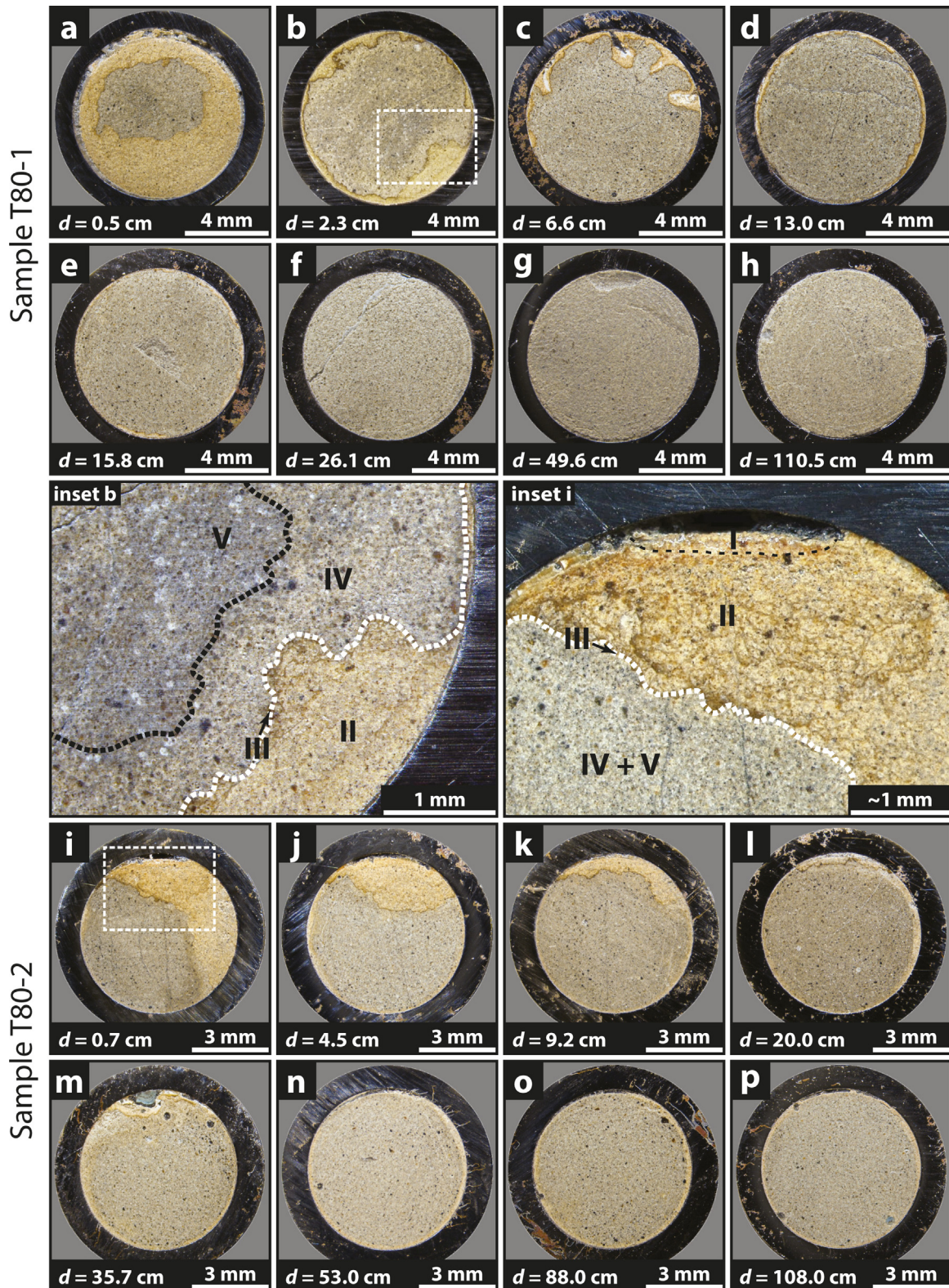
Fig. 5. Reflected light photographs of successively more distant cross-sections through coiled samples T80-1 (a-h) and T80-2 (i-p). Distance *d* [cm] from the upstream inlet is indicated for each section.

due to extensive local yielding of the steel tube, sustained during hydraulic debonding (Section 2.1). The diameter of the cement core appeared relatively unchanged (∼6 mm, i.e. factory ID of steel tube). Along the remainder of the coil length (*d* > 2 cm), the debonding aperture was much smaller (Fig. 3, insets), being about 60 μm

wide and fairly uniform in both tangential and axial (longitudinal) directions, though with local excursions in the range 40–95 μm.

Debonding at the cement-steel interface of sample T60-2 (Fig. 4) was less symmetric, with the cement core being off-centre in some of the sections studied. The debonding defect was about 20–50 μm
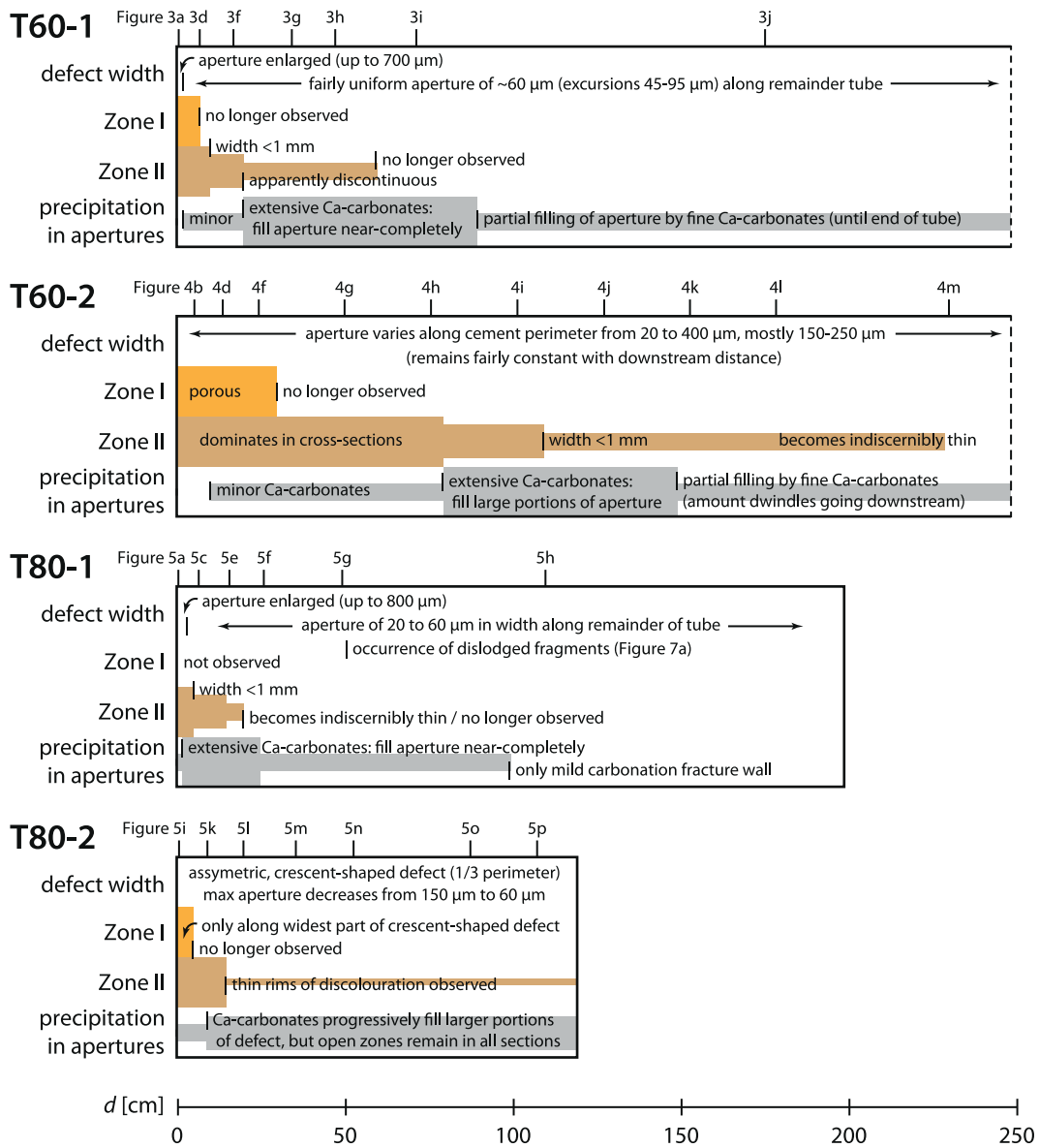
Fig. 6. Simplified graphical representation of the descriptions of defect geometry, cement alteration zonation and precipitation in the (debonding) defects given in the text (see Section 3.2.1). Vertical bars accompanying textual information indicate that the text applies to downstream of this bar.

wide where the cement core approached the tube wall and attained 200–400 μm at its widest point. The gap width was generally about 150–250 μm along half to three-quarter of the cement perimeter. This defect geometry remained fairly constant along the 6 m of tube.

Sample T80-1 (Fig. 5a–h) resembled T60-1 in having a more or less radially symmetric defect geometry, as well as showing marked widening of the debonded annulus to produce an annular gap of up to 800 μm within ~3 cm of the inlet. Along the remainder of the tube's length, the circumferential defect measured 20–60 μm in width. At distances greater than about half a metre from the inlet, the aperture locally contained cement fragments dislodged from the core (Fig. 7a). Where present, fragments typically occupied <30% of the perimeter of the cement core, the remainder of the debonding defect remaining unrestricted.

Sample T80-2 (Fig. 5i–p) showed a pronouncedly asymmetric defect geometry, in the form of a longitudinally continuous (or near-continuous), crescent-shaped void (Fig. 5i). This cavity may have formed due to gravitational-settling of the cement slurry in the curing stage, during which sample T80-2 (only) was stored on its side. Defects of such a nature may be relevant for inclined well-

bores. In proximal cross-sections (within ~20 cm of the upstream inlet), the aperture measured ~200 μm at the widest point of the "crescent", tapering off along within ~3 mm along the perimeter of the cement, towards a residual debonding aperture, some 10–20 μm wide, present along the entire remaining perimeter (Fig. 7b). This cross-sectional defect geometry remained fairly constant in the longitudinal direction, though the maximum aperture of the crescent-shaped opening gradually decreased to ~60 μm at the downstream end of the coil.

In all four samples, much larger, but short-ranged voids were locally present as well (e.g. Figs. Fig. 33g, Fig. 55m). Given their size and mostly spherical outline, these presumably represent air bubbles trapped during emplacement of the cement slurry.

3.2.1.2. Cement alteration and zonation. All samples showed similar results with regard to chemical alteration and zonation in the cement. In all cases, at least three, sometimes five distinct radial (i.e. sub-concentric) zones were observed in the cement matrix (Figs. 3–5). In the longitudinal direction, evidence of reaction and zoning tapered out rapidly, with the maximum downstream extent
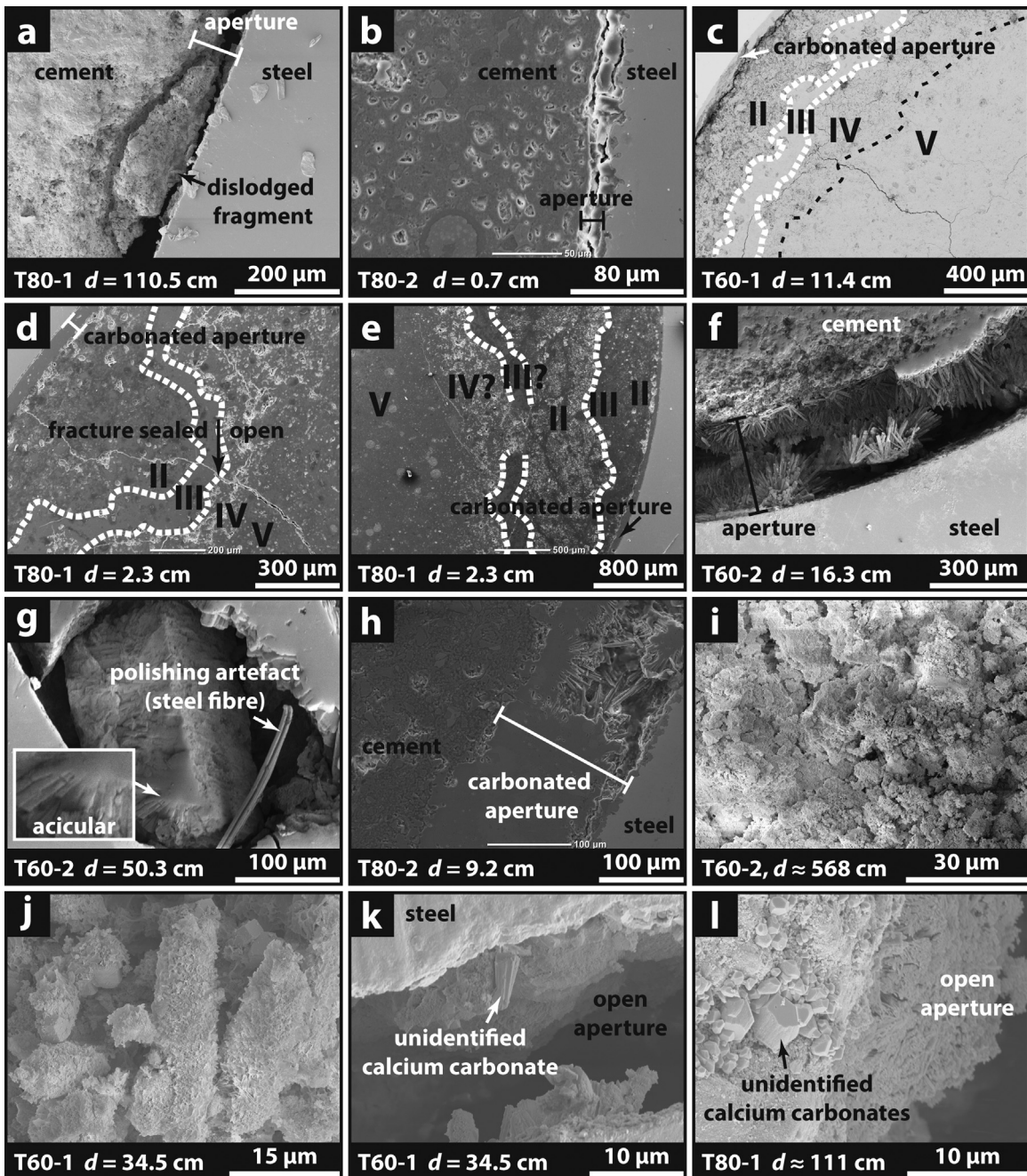
Fig. 7. Secondary electron SEM micrographs (unless indicated otherwise) of coiled sample cross-sections. Sample name and distance from the fluid inlet are as indicated. (a) cement fragment dislodged and obstructing the debonding defect in sample T80-1; (b) small debonding defect in sample T80-2; (c) Back-scatter electron image of reaction zones I–V in coil sample T60-1. Note the relatively dense and porous appearances of Zones III and IV, respectively; (d) fracture in sample T80-1, sealed by calcium carbonates in Zones II–III and open in Zones IV-V; (e) complex zonation pattern showing apparent repetition of Zone II in T80-1; (f) aragonite precipitation in debonding defect, sample T60-2; (g) micrograph of the material seen in the inset of Fig. 4g, showing its acicular nature; (h) precipitation of acicular crystals in sample T80-2; (i) fine-grained precipitate in debonding defect, sample T60-2; (j) detailed view of cement at the inner wall of the large pore visible in Fig. 3g, showing small rhombohedral crystals; (k, l) unidentified calcium carbonates precipitated in cement exposed in debonding defect, sample T80-1.

varying from ∼20 cm in T80-1 to ∼200 cm in T60-2 (Figs. 3–5). In the following, we first describe the general sequence of alteration zones, as encountered in the radial direction, and then present our observations on how the character and extent of this zonation change in the longitudinal direction, i.e. downstream.

In proximal cross-sections, which typically contained more complete successions of the alteration zones identified, the cement directly adjacent to the debonded cement-steel interface showed a relatively porous, orange band (referred to here as Zone I). This zone was up to ∼300 μm wide in the most proximal sections stud-

ied. It was developed mainly along sectors of the cement core perimeter where the defect aperture was largest (e.g. Figs. Fig. 3 3a, Fig. 4 4b, Fig. 5 5i + insets), but quickly diminished in downstream cross-sections. Moving towards the centre of the cement core, Zone I was followed by a less porous, orange-brown band (Zone II). The width of this zone averaged about 1–2 mm, but also varied considerably, locally ranging from ∼100 μm to >3 mm wide (e.g. Figs. Fig. 3 3a,b, Fig. 4 4a,b). Zone II was in turn followed by a sharply defined, thin (typically ∼100 μm wide), dark greyish to brownish front (Zone III – e.g. Figs. Fig. 3 3d, Fig. 4 4b, Fig. 5 5b,i + insets), which

appeared dense, i.e. of low porosity, in SEM images (Fig. 7c–e). Small sub-radial fractures, seen in all samples, were sealed where they traversed Zones II and III, but remained open deeper into the cement (Fig. 7d). This suggests that significant precipitation of carbonates (identified using EDX) occurred within the orange-brown and dark greyish zones (II–III). In SEM images of proximal cross-sections, areas of increased porosity could be observed inward of the dark greyish front of Zone III, suggesting that some reaction occurred in this region, which we shall hence denote Zone IV (Fig. 7c–e, see also Fig. 5b + inset). The grey-coloured remainder of the cement matrix (Zone V) generally appeared unaffected by reaction (e.g. Fig. 3g–l + insets). Interestingly, several of the cross-sections displayed a more complex zonation pattern, with apparent repetition of Zones II–IV, or additional high porosity regions located near the main defect (Fig. 7e). These complexities perhaps reflect the increases in fluid pressure difference that were imposed during the experiments, or may stem from the sectioning of three-dimensionally complex reaction front geometries.

In the downstream direction, the radial alteration zones seen in proximal sections thinned rapidly. Orange Zone I persisted up to about 7 cm, 30 cm and 5 cm downstream of the inlet in samples T60-1, T60-2 and T80-2, respectively. It was not observed at all in sample T80-1. The thinning out of orange-brown Zone II was most pronounced in coils T60-1 and T80-1, where it became <1 mm wide in cross-sections beyond 10 cm from the inlet and started to appear discontinuous from around 15–20 cm downstream (Figs. 3 and 5). The orange-brown colouration became indiscernibly thin at about 20–60 cm from the inlet. In sample T80-2, Zone II retained millimetre-width further downstream (up to ~15 cm), though only directly adjacent to the crescent-shaped void. Thin rims of discolouration were observed along the entire 1.2 m length of sample T80-2. In sample T60-2, Zone II dominated up to ~80 cm away from the inlet and remained millimetre-width up to ~110 cm (Fig. 4), finally tapering out somewhere between 180 and 230 cm downstream. The maximum downstream extent of dark greyish Zone III was more or less equal to that of Zone II, while that of the more porous Zone IV was difficult to assess.

3.2.1.3. Precipitates developed in interfacial apertures. In addition to the reaction zonation and radial crack sealing features seen in the cement matrix, cross-sectional observations revealed extensive precipitates of calcium carbonate (identified using EDX) formed in the open apertures at the cement-steel interfaces present in all samples. In samples T60-2, T80-1 and T80-2, radiating aggregates of acicular aragonite precipitate were observed (Fig. 7f–h). This acicular aragonite occurred locally in coil sample T60-1 also, but here most of the aperture-fill consisted of a fine-grained (mostly sub-micron sized), porous white precipitate. Similar fine material was also observed in samples T60-2 (Fig. 7i), T80-1 and T80-2. SEM-EDX analysis showed that these fine precipitates consisted mostly of calcium carbonate. The steel tube side of the interfacial defects was generally coated by a very thin corrosion scale, but otherwise did not show signs of reaction.

In the longitudinal direction, i.e. along the overall flow-path, the spatial distribution of the various calcium carbonate precipitates varied with downstream distance and between the four coil samples. In sample T60-1, only sparse precipitation was observed in apertures present in the first centimetre of the cement-filled coil. The cement here appeared extensively reacted and porous (Zone I, Fig. 3a + inset), while the diameter of the cement core had remained more or less unchanged. At a distance of ~2 cm from the inlet, calcium carbonates (identified using EDX) started to block up the debonding aperture, while the adjacent cement was still orange-brown coloured (Fig. 3d). Acicular aragonite occurred only occasionally. The extent of aperture-filling precipitation was largest and appeared near-complete somewhere between 20 and

90 cm downstream from the inlet (Fig. 3g–h). In more distal cross-sections (Fig. 3j–l), the interfacial apertures were only partially filled, predominantly with fine-grained calcium carbonates, while the adjacent cement appeared little altered (Zone V). Precipitates occurred in similar, slightly decreasing amounts up to the end of the 6 m tube.

In sample T60-2, cross-sections obtained from within about 10 cm of the inlet displayed only sparse to zero precipitation in the large open apertures, which instead were bounded by porous, bright orange, extensively altered cement (Fig. 4b). The sparse precipitate observed over this range mainly consisted of fine-grained, whitish material, presumably calcium carbonate. Further downstream, radial aggregates of acicular aragonite progressively fill the debonding defect (Figs. Fig. 4 4g, Fig. 6 6f–g). The extent of aragonite-filling was greatest between 80 and 150 cm away from the inlet, quickly dwindling to insignificant amounts further downstream. There, the debonding defect largely remained open, though often contained patches of fine white precipitate. The cement exposed at the open defects was partially carbonated, showing small idiomorphic crystals identified using EDX (Fig. 7i).

In sample T80-1, acicular aragonite was abundant in the most proximal cross-sections studied, with the characteristic crystals bridging large parts of the ~240 μm wide debonding defect present. Further downstream, where the debonding aperture narrowed, acicular aragonite and other (fine) carbonates filled the gap almost completely (Fig. 7d). At distances from the inlet greater than ~1 m, little evidence was found for precipitation in the apertures, for chemical zonation in the cement matrix, or for other changes beyond mild carbonation (Fig. 7l).

In the first ~9 cm sample T80-2, only the narrow, tapered ends of the crescent-shaped opening present here showed signs of precipitation of mixed calcium carbonates, while the centre of the defect remained open (Fig. 5i). The cement directly adjacent to the open aperture showed an increase in porosity and looked abraded (cf. sample T60-2). At distances beyond ~9 cm from the inlet, undiscerned calcium carbonates progressively filled the interfacial aperture (Fig. 7h), though more or less open patches remained present in all cross-sections studied from the remaining ~1.1 m.

3.2.2. Chemical analyses

3.2.2.1. Micro-X-ray fluorescence element maps. Single-element μXRF maps are shown in Fig. 8, for Fe, Ca, Si and S, as measured in selected polished sections of samples T60-1 and T80-2. The greyscales appearing in these images broadly reflect element abundance, with lighter shades corresponding to higher concentrations. Note that the spatial resolution of this method is about 30 μm only (spot size).

In general, the μXRF data confirm the reaction zonation seen using optical and SEM microscopy, though the azimuthal orientations of the cross-sections in Fig. 8 differ compared with Figs. 3–6. This zonation is particularly apparent in the sulphur maps, where S depletion correlates well with the extent of the orange and especially orange-brown colouration (Zone I and II, respectively) in reflected light micrographs. In mapping Ca, the highest concentrations were obtained where carbonates filled wide apertures at the cement-steel interface. Other reacted regions, such as the optically orange-brown coloured and dark greyish regions (Zone II and III, respectively) also showed elevated Ca concentrations. Lower Ca concentrations were found in the high porosity regions of Zone IV. Significant Ca-depletion was also observed immediately adjacent to the widest part of the crescent-shaped cavity in sample T80-2. The Si maps for T60-1 and T80-2 showed increased relative abundances of Si at locations near debonding defects, where the cement was substantially altered. The steel tube inevitably formed a prominent feature in all Fe maps. In addition, close to the inlet of both samples, Fe concentration was enriched in narrow zones within
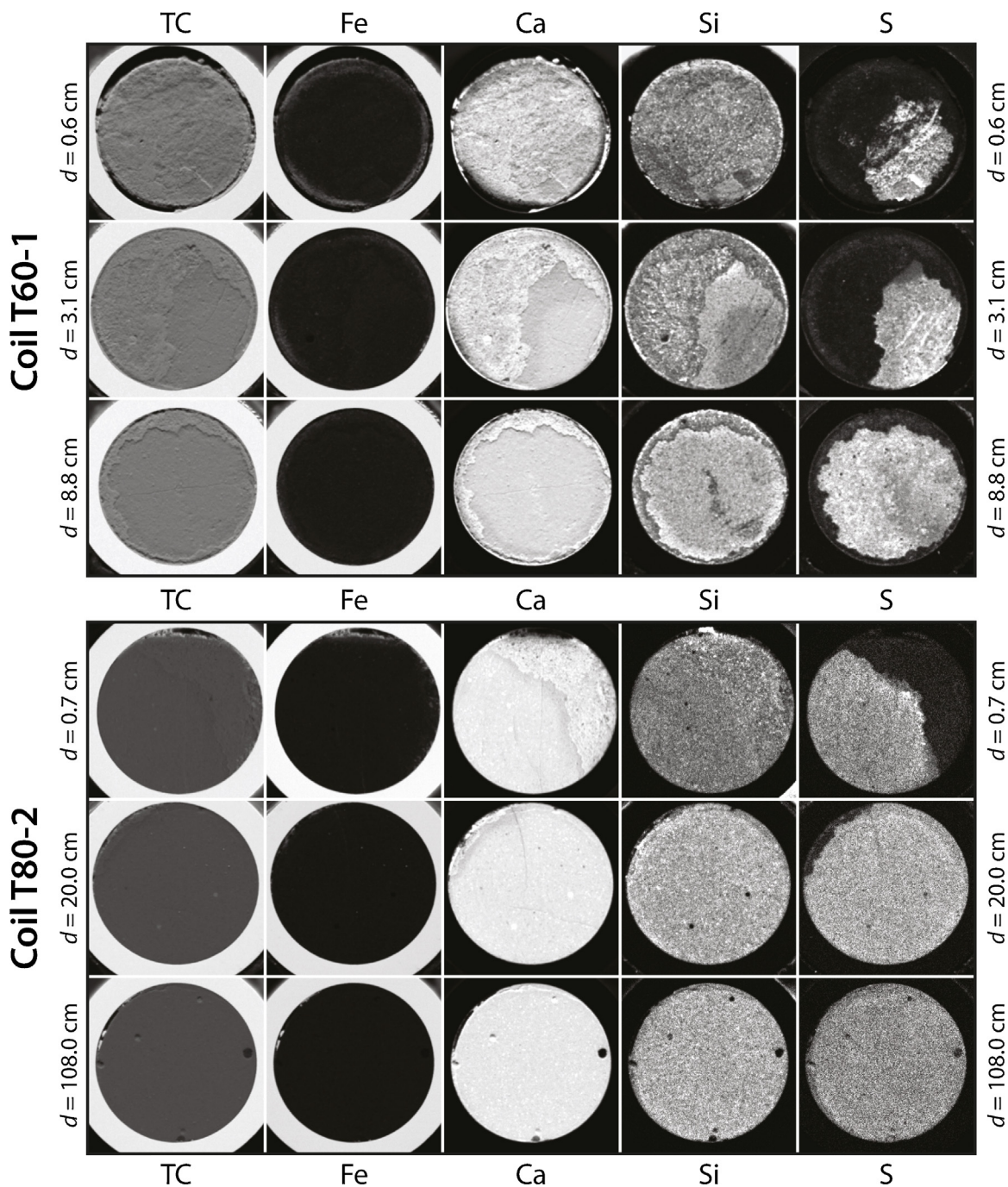
Fig. 8. Single-element micro-X-ray fluorescence maps of cross-sections of coiled samples T60-1 and T80-2. Distance *d* [cm] from the upstream inlet is indicated for each section. TC denotes total count maps. Greyscale is redefined per section and per element, and broadly reflects element abundance, with lighter shades corresponding to higher concentrations.

the cement bordering debonding defects. This was not observed further downstream.

3.2.2.2. X-ray diffraction data. Both XRD and TGA analysis were performed on the crushed hence averaged contents per sequential segment cut from the coiled tubes. The content of each reference sample was similarly treated. In all four coiled samples, as well as the reference samples, calcite, aragonite, vaterite, portlandite, gibbsite, ettringite and brownmillerite were identified qualitatively using XRD. Quantitative XRD analysis was performed only for calcite, aragonite and vaterite, to obtain estimates for the relative abundances of these calcium carbonate phases. No further quan-

tification was attempted, as Portland-based cements consist largely of poorly crystalline calcium silicate hydrate phases, which cannot be unambiguously identified using XRD techniques (Taylor, 1992). Quantitative XRD analysis of the reference cement samples yielded about equal amounts of aragonite, calcite and vaterite in all cases (e.g. 31.6, 34,4 and 34,0 wt%, respectively, in the reference equivalent of T60-1), probably reflecting low total calcium carbonate content rather than real polymorph distributions.

Turning to sample T60-1, quantitative XRD analysis was performed on three coil segments, obtained at 9 cm, 22 cm and 100 cm downstream of the inlet. In these, the aragonite content was highest in the sample from nearest the inlet (43.1 wt% at 9 cm), decreasing

to 37.1 and then 24.9 wt% at 22 cm and 100 cm. Calcite and vaterite content increased with downstream distance, from 39.8 to 43.8, and from 17.12 to 31.3 wt%, respectively. Further analysis was performed on a sample consisting of orange to orange-brown material (Zones I + II) only, obtained from ∼2 mm downstream of the inlet to sample T60-1. This consisted of 23.7 wt% aragonite, 63.6 wt% calcite and 12.7 wt% vaterite. In the case of sample T60-2, XRD analysis performed at 16 and 50 cm downstream of the inlet gave similar results, with aragonite, calcite and vaterite constituting 59.4, 19.9 and 20.7 wt%, respectively. In the case of T80-1, we obtained 48.2, 27.4 and 24.4 wt% of aragonite, calcite and vaterite, respectively, at 6 cm downstream. At 16 cm downstream, aragonite, calcite and vaterite constituted 30.7, 49.3 and 20.0 wt% of the carbonates in the coil segment. The carbonate composition of sample T80-2 in the range 10–16 cm was 39.3 wt% aragonite, 36.6 wt% calcite and 24.1 wt% vaterite. While the number of analyses is limited, these XRD results suggest that calcium carbonate was present in similar mineralogical proportions in the four coiled samples. From a comparison with our observations on defect configuration/fill and chemical zonation, the results also indicate that aragonite, and, to a lesser extent, vaterite, occurred preferentially in the debonding defects, while calcite dominated in the orange-brown zones (Zones I + II).

3.2.2.3. Thermo-gravimetric data. The TGA curves obtained for all coiled samples were typical for carbonated cement. The bulk of the weight loss occurred in roughly three stages (cf. Liteanu and Spiers, 2011; Luquot et al., 2013). In Stage 1, i.e. at temperatures below 350 °C, loss of free water and the dehydration of AFm, AFt and C-S-H phases dominated (cf. Hidalgo et al., 2008; Taylor, 1992). The second stage of weight loss, occurring over the temperature range 425–500 °C, could be mainly attributed to the dehydration of portlandite (Ca(OH)$_2$), (Taylor, 1992). Stage 3 weight loss, above 600 °C, was mainly due to the decomposition of calcium carbonates (cf. Hidalgo et al., 2008; Taylor, 1992; Villain et al., 2007), with perhaps some contribution from the final stages of dehydration of C-S-H and hydrated aluminate cement phases (Taylor, 1992). From the data obtained above 350 °C, weight percentages of Ca(OH)$_2$ and CaCO$_3$ were calculated in terms of CaO equivalents (Taylor, 1992).

For the unreacted (20 cm) reference cement samples corresponding to samples T60-1, T60-2, T80-1, and T80-2, portlandite contents of 16.8, 16.6, 18.5, and 16.9 wt% (±1 wt%) were obtained. This is typical for Class G HSR Portland cement (Lothenbach et al., 2008; Taylor, 1992). Calcium carbonates constituted 4.8, 6.1, 4.5 and 4.7 wt% (±3 wt%) of the four reference samples.

Turning now to the four coiled samples, Fig. 9 shows profiles depicting changes in the Ca(OH)$_2$ and CaCO$_3$ content with distance from the inlet. These profiles were constructed using the TGA data obtained from consecutive tube segments, measuring Ca(OH)$_2$ and CaCO$_3$ content relative to (i.e. in excess of) the reference sample values. All four coiled samples showed a decrease in portlandite content (dashed curves) of ∼4–10 wt% relative to the reference samples within the first ∼15 cm of the cement-filled tubes (Fig. 9). This decrease was mirrored by an increase in calcium carbonate content (continuous curves) of 10–30 wt%, or even ∼40 wt% in material from the upstream extremity of sample T80-1. Beyond about 15 cm from the inlet, the concentration profiles of the four experiments diverge. In sample T80-1, the portlandite content recovered over a short distance, attaining concentrations comparable to the unreacted cement beyond ∼20 cm from the inlet (Fig. 9b). Over the same range, the calcium carbonate content returned to a more-or-less constant value close to that of the reference cement. Similar behaviour was observed in samples T60-1 and T60-2, where changes in composition became negligible within ∼70 cm and ∼230 cm from the inlet (Fig. 9a). In the shortest sample T80-2 (1.2 m length), a decrease in portlandite and an increase in

calcium carbonate content were found along the entire longitudinal extent of the tube (Fig. 9b).
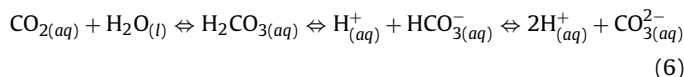
4. Discussion

The present results on our four, cement-filled, steel coils have shown that, while initial flow-through of water had no effect on apparent permeability, subsequent introduction of CO$_2$-rich fluid caused a reduction by several orders over two to three days of flow (Fig. 2). The largest decreases occurred in samples T60-1 and T80-1, where the apparent permeability dropped ∼4 orders, reaching the lower measurement limit of the permeameter. These samples contained debonding defects characterized by apertures <100 μm in width. By contrast, samples T60-2 and T80-2, which contained defects of 100–300 μm in width, showed a reduction of only 2–3 orders. Post-mortem analysis of all samples showed radially (sub-concentrically) zoned alteration of the cement, particularly near the CO$_2$ inlet, and precipitation of calcium carbonates in the cement-steel interfacial defects present, especially downstream. The distribution, extent and nature of the alteration zones and precipitates varied not only with downstream distance from the injection point of CO$_2$-bearing fluid, but also with defect width (Figs. 3–9). Both chemical and microstructural observations suggest that steel corrosion played little role. Comparing the experiments conducted at 60 and 80 °C, effects of temperature also seem to have been minor. In the following, we will discuss these results and attempt to explain the general trends seen, as well as the differences between the four reactive flow-through experiments. We further compare our data with previous experimental and modelling results on reaction and transport in fractured cement and within steel-cement interfaces. Finally, we consider the implications of our results for well integrity in the context of CO$_2$ storage.

4.1. Reactive transport mechanism

The present experiments showed no change in sample permeability during initial flow-through of water only, suggesting little or no reaction at the interface between cement and steel or in the cement matrix at this stage. This is consistent with previous experiments on cement plus water (e.g. Engkvist et al., 1996). The rapid drop in permeability observed when flow of CO$_2$-rich fluid was initiated, coupled with the radial and longitudinal chemical zonation and precipitation patterns observed after testing, clearly point to this stage of the experiments being dominated by upstream dissolution of cement via reaction with CO$_2$, followed by downstream precipitation of carbonates. Here, we evaluate this hypothesis in detail, making use of previous work. As our chemical and microstructural observations indicate that steel corrosion played only a minor role, we will focus on CO$_2$-cement reactions (corrosion will be discussed in Section 4.4).

A large body of literature exists regarding the chemical alteration of cement exposed to CO$_2$-bearing fluids. Reaction initiates as CO$_2$ dissolves in the pore fluid, leading to the formation and dissociation of carbonic acid.

$$CO_{2(aq)} + H_2O_{(l)} \Leftrightarrow H_2CO_{3(aq)} \Leftrightarrow H^+_{(aq)} + HCO^-_{3(aq)} \Leftrightarrow 2H^+_{(aq)} + CO^{2-}_{3(aq)}$$

(6)

In response to acidification, cement alteration in both open and closed systems involves dissolution of the portlandite and decalcification of the calcium silicate hydrate (C-S-H) phases present, producing (re-dissolvable) calcium carbonates and poorly crystalline alumino-silicates (Barlet-Gouédard et al., 2009; Kutchko

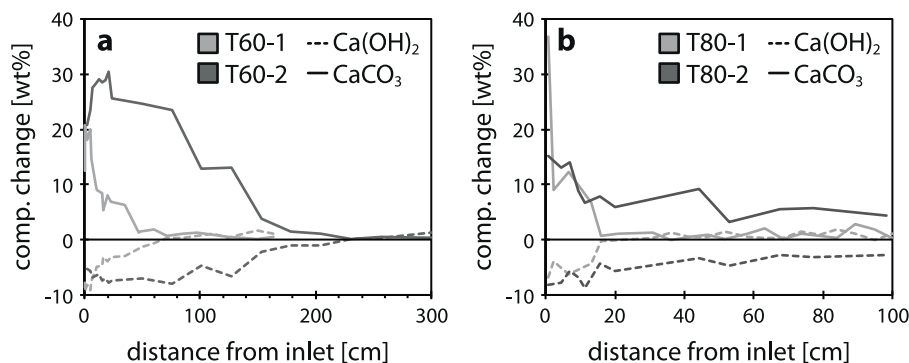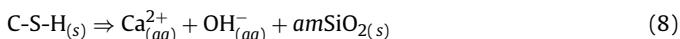**Fig. 9.** Profiles showing change in $Ca(OH)_2$ and $CaCO_3$ content of the cement core of the coiled samples, relative to virgin cement, as a function of downstream distance from the fluid inlet, data obtained from TGA analysis. Compositional change is defined here as the difference between measured composition and that of unreacted reference material.

et al., 2009, 2008, 2007; Mason et al., 2013; Rimmelé et al., 2008; Wigand et al., 2009), via the reactions (Kutchko et al., 2007).

$$Ca(OH)_{2(s)} \Rightarrow Ca^{2+}_{(aq)} + 2OH^-_{(aq)} \tag{7}$$

$$C\text{-}S\text{-}H_{(s)} \Rightarrow Ca^{2+}_{(aq)} + OH^-_{(aq)} + amSiO_{2(s)} \tag{8}$$

$$Ca^{2+}_{(aq)} + CO_3^{2-}_{(aq)} \Leftrightarrow CaCO_{3(s)} \tag{9}$$

From the CO_2-exposed surface of the cement to its interior, these reactions produce the following widely recognized sequence of alteration zones: (Z1) an orange-coloured, extensively reacted, porous zone, dominated by amorphous alumino-silicates, (Z2) an orange-brown zone characterized by the presence of mixed calcium carbonates, (Z3) a dense carbonation front, (Z4) a portlandite-depleted zone, and finally (Z5) apparently unreacted cement (Kutchko et al., 2007; Mason et al., 2013; Wigand et al., 2009). Zones Z2–Z5 are also reported in field studies where CO_2-exposed cement has been recovered from depth (Carey et al., 2007). The present experimental observations on tube cross-sections (see Figs. 3–8) match this general sequence, with our Zones I–V corresponding to Z1–Z5 above. In addition to the features of these zones established in literature, we observed loss of S and Al in our Zones I + II (Fig. 8). Similar changes were seen by Wolterbeek et al. (2016) in fractured cement samples reacted with supercritical CO_2-rich water. Wigand et al. (2009) also report depletion in Al, going from ~3.8 wt% Al_2O_3 (initial cement) to ~3.1 wt% (Z2 material) in their experiments. In this context, we note that the Fe-bearing AFm phases in cement are typically colourless (Taylor, 1992), supporting the notion that release of Fe^{3+} from a reacting mono- or tri-sulphate phase, producing iron hydroxide, may be responsible for the orange-brown colouration typical of altered cement (cf. Carey, 2013).

The chemical zonation discussed above has been widely recognized as an expression of the fact that CO_2-cement interactions are generally diffusion-controlled in the cement matrix (Geloni et al., 2011; Raoof et al., 2012), which inevitably generates concentration gradients in the internal pore fluid phase. In a system where the fluid is flowing through a defect, reaction will additionally lead to gradients in fluid composition in the flow-path direction (cf. Huerta et al., 2011). With reference to Eqs. (7) and (8), this is because dissolution of portlandite and de-calcification of the C-S-H phases progressively release Ca^{2+} into solution, increasing its concentration downstream. At the same time, due to the associated OH^- production and pH buffering to alkaline values (Eqs. (7), (8)), the carbonic acid equilibria in Eq. (6) are gradually shifted towards the right-hand side, generating (bi)carbonate at the expense of dissolved CO_2. Ultimately, precipitation of calcium carbonates will occur somewhere downstream, via Eq. (9), provided sufficiently high Ca^{2+} and CO_3^{2-} concentrations can be attained. If the flow-rate

is high and the sample short (<2 cm), no significant precipitation will occur (Abdoulghafour et al., 2013; Luquot et al., 2013). However, given the length scale of our samples and of real well systems, sufficiently high concentrations might result in precipitation and self-sealing (Brunet et al., 2016; Cao et al., 2015; Deremble et al., 2011; Huerta et al., 2016).

Our microstructural observations, made using samples of 1.2–6.0 m in length, fit well with this conceptual model of dissolution-dominated reaction near the CO_2 source/inlet, followed by a transition to precipitation-dominated reaction downstream. The extent of orange-brown colouration (Z1 + Z2) diminishes with downstream distance in all of our samples (Figs. 3–6), suggesting a reduction in the extent of CO_2-alteration. Moreover, fully leached cement (Zone I = Z1), like that observed in experiments exposing cement to either large volumes (Duguid et al., 2011; e.g. Kutchko et al., 2007) or large fluxes of CO_2-bearing fluid (Abdoulghafour et al., 2013; Luquot et al., 2013; Mason et al., 2013), was observed only in the first 1–30 cm of our coil samples, where the cement was Ca-depleted and Si-enriched (Fig. 8). This leached cement was also structurally degraded (porous) along the widest parts of debonding defects (Figs. Fig. 33a, Fig. 44b). The present TGA data also indicate that dissolution occurred mainly upstream, as significant portlandite depletion was confined to the upstream half of the coiled samples (Fig. 9). Calcium carbonate precipitates were occasionally observed in open defects close to the inlet (Figs. Fig. 33a, Fig. 44b, Fig. 55i). However, they occurred extensively further downstream (Figs. 3–7). The TGA data on calcium carbonates is consistent with this but represents volumetric averages, thus incorporating carbonation within the cement matrix as well as precipitation in defects (Fig. 9).

On this basis, we infer that the broad picture of dissolution/precipitation seen in our experiments is consistent with a reactive transport mechanism involving upstream dissolution of portlandite and de-calcification of C-S-H phases, producing amorphous silica (Zone I) and buffering the fluid pH, followed by saturation of this fluid and precipitation of carbonates downstream. The mechanism pictured is illustrated diagrammatically in Fig. 10, in relation to our key observations and the reactions inferred to occur.

4.2. Permeability reduction mechanism

Having identified the mechanism responsible for cement-reaction plus carbonate precipitation in defects, we now consider whether this precipitation process can account for the observed permeability reduction. First, it is important to note that the measured initial (water) permeability of all samples was 3–5 orders of magnitude higher than that of the cement matrix (typ-
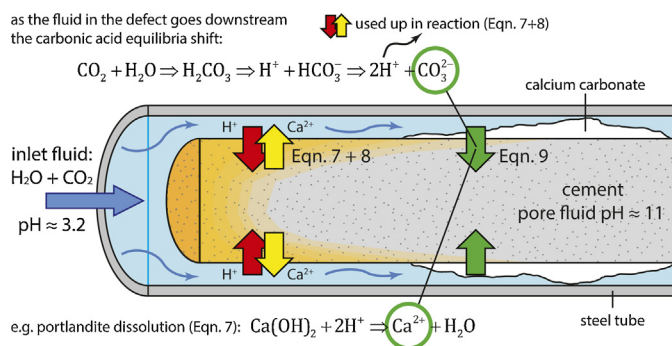
Fig. 10. Diagrammatic representation of the reactive transport mechanism discussed in Section 4.1.

ically 10^{-21}–10^{-17} m^2, cf. Montgomery, 2006; Taylor, 1992) and, accordingly, of the fractured cement segments that likely formed during coil bending (samples T60-1, T60-2 and T80-1). This means that the observed initial permeability must reflect flow through the (debonding) defects at the cement-steel interface and that subsequent permeability reduction must be related to processes restricting flow within these defects.

The most obvious such process is indeed the precipitation of calcium carbonates, observed in all coil samples. However, much of the precipitate was acicular aragonite, which has previously been interpreted as a degassing feature in open fractures in natural CO$_2$ reservoirs (Kampman et al., 2012). We therefore need to consider to what extent the observed carbonates and permeability reduction could be related to degassing of the CO$_2$-rich fluid during flow or during depressurization upon experiment termination. A decrease in permeability could be related to degassing of CO$_2$, due to the decrease in fluid pressure along the flow path or changes in salinity. This would lead not only to carbonate precipitation but also to multi-phase flow and relative-permeability effects (e.g. Bear, 1972). Both have previously been invoked as a partial cause of apparent permeability reduction in cement samples exposed to CO$_2$ (Bachu and Bennion, 2009; Newell and Carey, 2012). Degassing might also reduce flow via increases in dynamic viscosity due to decrease in CO$_2$ content (Islam and Carlson, 2012) or coupled changes in salinity (Mao and Duan, 2009). However, in the present experiments the upstream CO$_2$-bearing fluid was prepared to guarantee under-saturation with CO$_2$ at downstream pressures (Section 2.3). This should have prevented significant CO$_2$ degassing during flow-through (assuming only minor changes in salinity and hence CO$_2$-solubility due to mixing of CO$_2$-rich fluid with resident pore water).

Other potential factors that may contribute to permeability reduction include (a) mechanical closure of defects due to chemical weakening of aperture-propping asperities (Huerta et al., 2009; Walsh et al., 2014b), and (b) dislodgement and migration of fines and alteration products, leading to clogging (Feia et al., 2015; Newell and Carey, 2012). Chemical weakening of asperities can be eliminated as no effective confining pressure or defect-normal stress was applied in the present experiments. Elastic deformation of the steel tube in response to internal fluid pressurization may have contributed to the transiently high permeability that followed each increase in ΔP imposed in our tests (Fig. 2). However, this cannot explain the subsequent decrease to lower permeability values.

Given our observations of cement fragments (Fig. 7a) and fine precipitates (Fig. 7i) locally obstructing debonding defects, dislodgement and migration of fines may have contributed to permeability reduction, especially since coil bending during preparation (Section 2.1) undoubtedly created such debris. However, all samples showed a stable permeability with respect to water

prior to the injection of CO$_2$-bearing fluid. Moreover, sample T80-2, which was coiled prior to cement curing and did not experience hydraulic debonding, behaved similarly to the other three samples (Fig. 2). This suggests that migration of fines required at least some degree of chemical alteration. Also, large apertures remained open in all cross-sections where fragmented material was observed (e.g. Fig. 7a). We therefore infer that blocking by fragments/fines may have contributed to, but cannot explain the major reduction in permeability observed.

By the above process of elimination, we conclude that the measured permeability evolution is primarily due to blocking by calcium carbonate precipitation within cement-steel interfacial defects during our reactive flow-through experiments, perhaps aided by migration of fines and alteration products. It also seem likely that acicular aragonite was at least one of the carbonate phases precipitated during reactive flow-through. This would be consistent with the fact that Crow et al. (2010) found abundant aragonite in cement samples recovered from a well in a natural CO$_2$ reservoir. Similarly, Carey et al. (2007) found a carbonated rind on cement obtained from the casing-cement interface of a well in the SACROC Unit, West Texas, that experienced 25 years of CO$_2$-enhanced oil recovery. This contained 60 wt% aragonite and 24 wt% calcite (Table 1 in Carey et al., 2007), i.e. proportions similar to those seen in our XRD data (Section 3.2.2.2). Aragonite precipitates were also observed by Wolterbeek et al. (2013) in batch reaction experiments on cement-steel composite samples employing a variety of CO$_2$-bearing fluids at $T = 80\,^\circ$C and $\sim$14 MPa applied CO$_2$ pressure. In that study, we postulated that aragonite formed, rather than calcite, due to presence of casing steel-derived Fe^{2+}, which is known to inhibit crystallisation of calcite (Al-Saiari et al., 2008). This body of evidence suggests that the acicular aragonite precipitation seen in the present experiments is a real permeability-reducing effect that can be expected to occur in cement-steel interfaces under in situ conditions. At the same time, we cannot eliminate the possibility that at least some of it formed due to degassing upon test termination (see also Wolterbeek et al., 2016).

4.3. Present results versus previous work on self-sealing in fractured cement

There is considerable variation among our coiled samples regarding the downstream extent of reaction and the final sample permeabilities attained (Table 1, Fig. 2). In general, the degree of alteration and reaction front depth increased with increasing aperture size (Figs. 3–9). At the same time, permeability reduction was much more pronounced in the two samples with defect apertures <100 μm (~4 orders decrease in T60-1 and T80-2), than in those having defects 100–300 μm in width (2–3 orders decrease in T60-2 and T80-2). The driving force for flow was similar in all four experiments, with the initial pressure differences applied corresponding to a pressure gradient of $\sim$0.1 MPa m^{-1}, i.e. $\sim$10 times hydrostatic. In this section, we will attempt to explain the variation seen in our coiled samples, by comparing the results with previous experiments and models of reactive transport of CO$_2$-rich fluids through fractured cement only.

4.3.1. Comparison with experiments

The aragonite and other calcium carbonate precipitates inferred to cause permeability reduction in our coiled samples during reactive flow-through, are similar to those found on the fracture surfaces of CO$_2$-reacted, fractured cement, as reported by Wigand et al. (2009) or Liteanu and Spiers (2011). These authors qualitatively associated carbonate precipitation with reduction in porosity and permeability. Other experimental studies on fractured cement have shown that permeability evolution at constant injection-rate (Abdoulghafour et al., 2013; Luquot et al., 2013), or constant pres-

sure difference driving flow of CO_2-rich fluid (Cao et al., 2015; Huerta et al., 2016), depends on the initial hydraulic aperture of the fractures, the sample length, and magnitude of the pressure difference or flow-rate imposed. Also these findings are in good agreement with our results.

4.3.2. Comparison with models

The above-mentioned experimental observations on fractured cement by Luquot et al. (2013) and Huerta et al. (2016) were recently captured in a reactive transport model by Brunet et al. (2016). This model confirmed that hydraulic aperture and specifically residence time (τ [s]), defined.

$$\tau = \frac{V_{defect}}{Q_{defect}} \qquad (10)$$

where V_{defect} is the void volume of the defect [m^3] and Q_{defect} is the fluid flux [m^3 s^{-1}], are key parameters in determining whether reactive flow of CO_2 along fractures will be self-sealing or not – see also models by Cao et al. (2015) and Abdoulghafour et al. (2016). The model predicts that narrow defects seal faster. Long residence times provide enough time for CO_2-rich fluid and cement to interact to the point where downstream pH and Ca^{2+} concentrations are sufficiently high for precipitation of carbonates, whereas short residence times do not. Based on their model simulations, Brunet et al. (2016) obtained the following relation describing the critical residence time (τ_{crit} [s]) for sealing of fractures in cement:

$$\tau_{crit} = \alpha_1 w_{hydr}^2 + \alpha_2 w_{hydr} \qquad (11)$$

Here, w_{hydr} [μm] is the hydraulic aperture of the defect, and α_1 plus α_2 are empirical constants with values of 5.88×10^{-2} [s μm^{-2}] and 15.24 [s μm^{-1}], respectively. If the residence time of CO_2-rich fluid in a cement fracture is larger than this critical value, τ_{crit} [s], then self-sealing is expected. The behaviour predicted by Eq. (11), is plotted in residence time versus hydraulic aperture space in Fig. 11.

To compare our results for the coiled samples with the Brunet et al. (2016) predictions for fractured cement represented in Fig. 11, estimates of the defect void volume (V_{defect}) and hydraulic aperture (w_{hydr}) of our samples are needed. These were made using both microstructural and permeability data, assuming $Q_{defect} \approx Q_{LRC}$. Defect volume was estimated from microstructure using $V_{defect} = \left(R_{tube}^2 - (R_{tube} - w_{obs})^2\right) \cdot L$, for samples T60-1, T60-2 and T80-1 (annular defect), and using $V_{defect} = \pi w_{obs} R_{tube} L/3$ for T80-2 (crescent-shaped void), where w_{obs} [m] is the average aperture of circumferential defects, as observed in the tube cross-sections (see Figs. 3–5, and Table 1), and L [m] denotes tube length (Table 1). Assuming $w_{hydr} \approx w_{obs}$ [μm] provided a first (upper bound) estimate of the hydraulic aperture. Estimates of V_{defect} and w_{hydr} were made from the permeability data assuming that flow occurred via a circumferential aperture represented by the region between two coaxial cylindrical plates with radii R_{cement} and R_{tube} [m]. The hydraulic aperture is then given by $w_{hydr} = R_{tube} - R_{cement}$ [m], and is related to sample permeability via (cf. Bird et al., 2002):

$$\kappa_{app} = \frac{1}{8R_{tube}^2}\left(R_{tube}^4 - \left(R_{tube} - w_{hydr}\right)^4 + \frac{w^2\left(2R_{tube} - w_{hydr}\right)^2}{\ln\left(1 - w_{hydr}/R_{tube}\right)}\right) \qquad (12)$$

Initial hydraulic apertures for the coiled samples, obtained using Eq. (12), plus initial κ_{LRC} and R_{tube} data, are given Table 1. These hydraulic apertures also provide a lower bound estimate of defect void volume, by assuming $V_{defect} = \left(R_{tube}^2 - \left(R_{tube} - w_{hydr}\right)^2\right) \cdot L$ for coiled samples T60-1, T60-2 and T80-1 (annular defect), and $V_{defect} = \pi w_{hydr} R_{tube} L/3$ for sample T80-2 (crescent-shaped void).
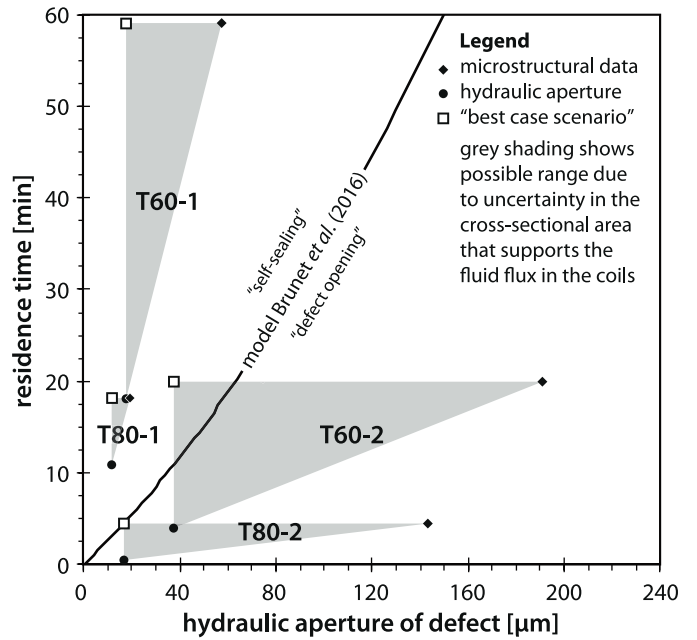

Fig. 11. Self-sealing and defect opening as predicted by the Brunet et al. (2016) model (Eq. (11)), plotted in residence time versus hydraulic aperture space, together with the four coiled samples, represented as grey triangles, which show uncertainty. For each triangle, the bottom-left corner, denoted with a solid circle, corresponds to the aperture and void volume determined from the permeability data. Similarly, top-right corners (solid diamonds) represent microstructural observations. Lastly, top-left corners, denoted by open squares, can be considered as "best case scenarios" for sealing in the coiled samples, combining the longer residence time estimated using the microstructural observations with the smaller hydraulic aperture, estimated from the permeability data.

We can now estimate the residence time of CO_2-bearing fluid in our coiled samples, plotting these in Fig. 11. The data for the four coil samples appear as grey triangles, representing uncertainty in the defect aperture and void volume as determined from microstructure (solid diamonds) versus permeability (solid circles). Open squares represent combinations of the smallest and largest estimates obtained of hydraulic aperture and defect volume, respectively, hence maximum sealing potential. Note that in all coiled samples, the apertures observed in cross-section (Figs. 3–5) were larger than the corresponding hydraulic apertures obtained from permeability data. This may reflect roughness due to cement fragmentation (Fig. 7a) or else local aperture or tube constrictions, both of which promote sealing by increasing residence time.

From Fig. 11, it is clear that the residence time in samples T60-1 and T80-1 was larger than the critical residence time predicted by the Brunet et al. (2016) model. This corresponds well with the continued permeability decrease observed in these samples (Fig. 2). By contrast, the residence-time/aperture estimates for samples T60-2 and T80-2 fall largely below the critical line defined by Eq. (11), consistent with the fact that these two samples remained relatively permeable compared to T60-1 and T80-1 (Fig. 2). These observations suggest that the Brunet et al. (2016) model, though developed for fractured cement, may also be applied to cement-casing interfaces, provided that corrosion reactions play a minor role. It should be noted, however, that the permeability decreases observed in the two samples that plot in the sealing-regime of Fig. 11 (T60-1 and T80-1) were considerably larger (3–4 orders) than the 1–2 orders predicted by the Brunet et al. (2016) model (see Fig. 8 of Brunet et al., 2016). Also, the two samples that plot in the defect opening-regime (T60-2 and T80-2) showed a limited permeability decrease, rather than defect opening. This may be related to a difference in reactivity of cement-steel interfaces compared to cement-cement fractures

(Brunet et al., 2016), or to effects of supercritical versus liquid CO_2, or to effects of local aperture constrictions. Most likely, however, the difference is because Eq. (11) was obtained from simulations conducted using chemical data (kinetic and equilibrium constants) and diffusion coefficient data that apply for 25 °C (Brunet et al., 2016). The effect on Fig. 11 of increasing temperature is likely a lowering of the critical residence time, since (a) CO_2-cement reactions are typically diffusion-controlled (e.g. Raoof et al., 2012), and (b) diffusion and advective transport rates probably increase similarly with temperature, due to the inverse relation between diffusion coefficient and dynamic viscosity embedded in the Stokes-Einstein equation (e.g. Zwanzig and Harrison, 1985). This coupling suggests sealing tendency may remain approximately the same with temperature, while residence time (for a given hydraulic aperture and pressure gradient) will go down due to a decrease in dynamic viscosity with increasing temperature. This temperature-dependent behaviour can perhaps be captured in future modelling work by incorporating the timescale of reaction, in addition to the timescale of transport, e.g. by using appropriate Damköhler Numbers (Abdoulghafour et al., 2016; Nogues et al., 2013).

4.4. Comparison with previous experiments on cement-steel interfaces

Considering the apparently minor role played by CO_2-induced steel-corrosion reactions, the present experiments seem at odds with previous investigations that address the cement-steel-CO_2-brine system (Choi et al., 2013; Han et al., 2012; Wolterbeek et al., 2013). Carey et al. (2010, 2009), for example, conducted a high-flux core-flooding experiment using a CO_2-brine (at $T = 40$ °C, $P_c = 28$ MPa, $P_f = 14$ MPa). Their sample consisted of a J55-steel bar embedded axially in a cement plug, with interfacial apertures ranging from 200 to 800 μm in width. They observed precipitation of poorly crystalline mixtures of Fe/Ca-carbonate dominated by corrosion products. Extensive corrosion scale also developed in batch reaction experiments conducted by Wolterbeek et al. (2013) on composite cement plus N80-steel samples, with interfacial aperture widths of 50–350 μm, immersed in CO_2-bearing fluids ($T = 80$ °C, $P_f = 14$ MPa). This scale formed on the exposed cement surface, inhibiting cement reaction and calcium carbonate precipitation (Wolterbeek et al., 2013).

Possible explanations for the comparatively minor role of corrosion scale formation in the present experiments include the following. First, we used different steel. Indeed, all the above studies employed different low-carbon mild steels (here ST.35, versus J55 and N80 in Carey et al., 2010 and Wolterbeek et al., 2013, respectively), the behaviour of which in CO_2-rich environments may differ. Second, the pre-test state of the steels varied. In the present experiments, the steel tube surface was preconditioned for a year during cement curing, potentially reducing reactivity. By contrast, pristine steel plates were used by Wolterbeek et al. (2013), while Carey et al. (2010, 2009) machined the steel bar to create interfacial apertures, creating freshly exposed surfaces. Third, differences in experimental configuration and (unconstrained) redox conditions may have affected the corrosion behaviour. Both Carey et al. (2010, 2009) and Wolterbeek et al. (2013) employed steel components that were fully surrounded by CO_2-bearing fluid. However, the steel tubes used in the present experiments were exposed to the fluid only at the internal wall. Since steel is a conductor, CO_2-induced electrochemical reactions (Dražić and Hao, 1982; Nešić, 2007) may therefore have produced long-range transfer of electrons, e.g. between different chemical environments along the flow-path or between the inside and outside of our tubes. Similar phenomena can be expected in real well systems, where the casing steel connects multiple formations bearing fluids of varying salinity and redox conditions. Lastly, the hydrodynamical conditions in the present experiments may have allowed for more effective protection of the steel by the cement (Choi et al., 2013). This would be in line with the increased Fe concentrations observed along debonding defects in proximal cross-sections of samples T60-1 and T80-2 (Fig. 8). The cement at this location was extensively reacted (Z1–Z2) and probably had lost its pH buffering capacity.

At present we cannot discriminate which of the above explanations is most likely for the apparent unimportance of corrosion reactions in our experiments. Moreover, given the variable results obtained in reaction experiments in general, there are currently insufficient data available to constrain the effects of corrosion scale formation on well system integrity in the field confidently. Additional research into the detailed interface reactions is required, including simulation of downhole electrochemical conditions and possible effects of long-range conduction.

4.5. Synthesis and implications for real well systems

The present permeametry and microstructural data suggest that progressive saturation of CO_2-bearing aqueous fluid, moving alongside defects in cement-casing interfaces, can lead to extensive downstream precipitation of calcium carbonates, effectively sealing debonding defects 20–100 μm wide. However, our data were obtained using pressure gradients ~10 times hydrostatic. If the pressure gradients in leaking wells are lower, residence times will be accordingly longer. With reference to Fig. 11, the implication is that long-range reactive transport processes may significantly contribute to the self-sealing potential of cement-interfaces in well systems. However, the present results and previous model work (Brunet et al., 2016; Cao et al., 2015; Deremble et al., 2011) show that sealing due to reactive transport is strongly dependent on the hydraulic aperture of the defects concerned, highlighting the long-recognized need for quantification of defect dimensions in real well systems (for which current monitoring methods provide only limited constraints). Nonetheless, for a good "cement job", curing-induced debonding apertures are estimated to be 10–20 μm in width (Dusseault et al., 2000). Assuming our experimental conditions apply to real wells, such defects can be expected to self-seal rapidly if CO_2-rich fluid begins to leak along them. Substantially larger defects may also show a reduction in permeability. However, more work is required to assess the long-term behaviour of defects that do not seal on experimental timescales. Noting that we observed limited permeability decrease in samples T60-2 and T80-2, while the Brunet et al. (2016) model predicts defect opening for these samples (Fig. 11), improved agreement between simulations and experiments can perhaps be obtained by including the effects of elevated temperature and steel reactions in future modelling formulations.

In addition, it should be noted that there are several factors that complicate comparison of our experiments with downhole situations. Most importantly, perhaps, is the nature of CO_2 leakage, which might involve supercritical or even gaseous CO_2, partially saturated with water, rather than CO_2-rich water. These could lead to dry-out and shrinkage of the wellbore cement. Furthermore, surface casing leakage of natural gas often displays a pulsing or periodic nature (Jackson and Dusseault, 2014). If CO_2 leakage were to occur in similar pulses (cf. Kampman et al., 2012), the transiently high flow-rates may impact chemical-hydrodynamic coupling in an unanticipated manner. This necessitates additional experiments investigating the effects of "bursts" of CO_2-bearing fluid on the self-sealing potential of cement-interface defects in well systems.

Further work is also needed to assess the impact of competition between sealing due to chemical reaction and possible reopening due to accompanying geomechanical effects. Local reduction in permeability will inevitably produce localisation of the fluid pressure gradient, i.e. lead to fluid pressure increase upstream and

decrease downstream of the low permeability region. Since interfacial defects and fractures are generally pressure dependent (e.g. Bernabe, 1986), readjustment of the fluid pressure gradient may lead to reopening of defects, e.g. via a hydraulic fracturing mechanism (Lecampion et al., 2013, 2011). Such phenomena may also explain transient increases in permeability observed in the present experiments after the US pump pressure was increased (Fig. 2), for this will similarly lead to a readjustment of the fluid pressure gradient along the cement-filled steel tube."

5. Conclusions

The aim of the present study was to investigate the effects of long-range reactive transport processes on the sealing-potential of CO_2-induced reactions in debonding defects at well casing-cement interfaces. To this end, we performed four reactive flow-through experiments on 1–6 m sections of simulated debonded cement-steel interface. The four samples were prepared by casting cement into (coiled) steel tubes (length 1.2–6.0 m, inner diameter 6–8 mm), which were pressurized after cement curing, causing the steel tube to deform permanently and to lift off the cement, creating debonded cement-steel interfaces. The experiments were performed using constant pressure differences in the range 0.12–4.6 MPa, temperatures of 60/80 °C, and fluid pressures of 10–15 MPa, continuously measuring the fluid flow-rate. Following experiment termination, the samples were sectioned at regularly spaced downstream intervals and subjected to microstructural and mineralogical analyses, using optical and scanning electron microscopy, X-ray diffraction analysis, micro-X-ray fluorescence spectroscopy and thermo-gravimetric analysis. The main findings can be summarized as follows:

1. During initial, water-based permeability measurement, all four coiled samples showed stable apparent sample permeabilities ranging from 1.0×10^{-13} to 3.3×10^{-12} m². Upon reactive flow-through with CO_2-bearing aqueous fluid, significant reduction in sample permeability occurred within about three days of measurement. The largest decreases occurred in two coiled samples having debonding apertures <100 μm, where permeability dropped ∼4 orders. The permeability decrease in the remaining two samples, which contained debonding defects 100–300 μm wide, was 2–3 orders.
2. Microstructural observations showed extensive cement alteration close to the upstream fluid inlet, with reaction zonation developed in accordance with that documented in the literature. However, the extent of cement alteration diminished steadily with downstream distance from the CO_2 source, with extensively altered, depleted-cement zones being absent beyond about 30 cm downstream. At the same time, extensive precipitation of calcium carbonate (aragonite, calcite and vaterite) occurred, especially downstream, obstructing considerable portions of the open apertures at the debonded cement-steel interfaces. These observations were substantiated by the XRD, μXRF and TGA results, which also showed dissolution-dominated cement alteration upstream and extensive precipitation further downstream. Steel corrosion reactions were very limited and played little or no direct role in the experiments.
3. Combining these observations, we conclude that the observed permeability reduction is related to the build-up of high Ca^{2+} and (bi)carbonate ion concentrations in the CO_2-bearing fluid, as it moves alongside the cement exposed at the defect surfaces. This leads to (super)saturated conditions with respect to calcium carbonate some distance downstream of the CO_2 source, resulting

in precipitation in the interfacial defects, thereby significantly decreasing permeability.

4. In this regard, our results imply that sealing of debonding defects at casing-cement interfaces in real wells is aided by long-range reactive transport, especially considering the length scale of cement seals in field situations (typically 10 s–100 s of meters). However, the present results and previous modelling work also show that self-sealing is strongly dependent on the hydraulic aperture of the defects involved. Small apertures (10–20 μm) can likely be expected to seal. Substantially larger defects may also show a reduction in permeability, but do not necessarily attain an impermeable state, More work is needed to assess the long-term behaviour of defects that do not seal on experimental timescales. Further work is also needed on possible well leakage involving transiently high, pulsing flow-rates, and on the potential effects of long-range electrical conduction on electrochemical casing corrosion.

Appendix A. Permeameter benchmarking

Prior to the reactive flow-through experiments, the functionality of the permeameter system was tested using a steel capillary tube, as a reference sample (length 1.36 m, ID 600 μm, loosely coiled-up to fit in the thermobath). The benchmark tests were performed at room temperature, using water, with either both syringe pumps in pressure control mode, or with the US pump in flow-rate control mode and the DS pump regulating back-pressure.

For flow in a capillary tube, the relation between ΔP [Pa], the pressure difference acting across the tube, and Q [m³ s⁻¹], the fluid flux through the tube, should conform to the phenomenological Darcy-Weisbach equation (e.g. Brown, 2002; Papaevangelou et al., 2010), here written in the form:

$$\Delta P = f_D \times \frac{\rho L}{4R} \times \left(\frac{Q}{\pi R^2} \right)^2 \tag{13}$$

where f_D denotes the Darcy friction factor [−] and ρ is the water density [kg m⁻³], while R and L denote the inner radius [m] and length [m] of the capillary tube, respectively. For the laminar flow-regime, the Darcy friction factor is given by (e.g. Brown, 2002):

$$f_D = \frac{64}{Re} \quad \text{with} \quad Re = \frac{2\rho Q}{\pi \mu R} \tag{14}$$

where Re denotes the Reynolds number for flow in a pipe [−] and μ the dynamic viscosity of the fluid [Pa s]. Note that combining Eqs. (13) and (14) results in the Hagen-Poiseuille equation for laminar pipe-flow (Hagen, 1839; Poiseuille, 1844; Sutera and Skalak, 1993). For the fully turbulent flow-regime, we adopted the Blasius correlation (Blasius, 1913; Brown, 2002; Trinh, 2010):

$$f_D \approx 0.316 Re^{-0.25} \tag{15}$$

which provides an easily implemented, yet adequate approximation for relatively smooth-walled pipes.
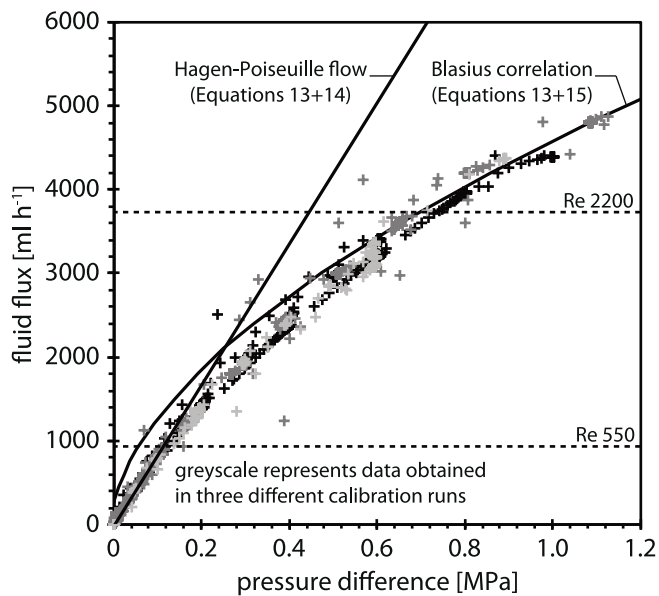
Fig. A1. Fluid flux versus pressure difference data (grey and black crosses), obtained during permeameter benchmark tests, performed on a capillary tube (length 1.36 m, ID 600 μm). Theoretical predictions for a capillary tube of these dimensions, made using the Hagen-Poiseuille equation (laminar flow) and Blasius correlation (fully turbulent flow), are also plotted. Dashed lines delineate these regimes, in terms of the Reynolds number (Re) of flow in the capillary tube.

Fig. A1 shows Q versus ΔP data for the capillary tube, measured in the permeameter system, together with curves predicted for the laminar and turbulent flow-regimes using Eqs. (11)–(13), using values of $1000\,\mathrm{kg\,m^{-3}}$ and $3\times10^{-4}\,\mathrm{Pa\,s}$ for the density and dynamic viscosity of water. Our experimental data correspond well with the Hagen-Poiseuille equation for Re < 550 (horizontal dashed line), a range similar to that found by Celata et al. (2002), who observed laminar flow in capillary tubes (ID 130 μm) for Re < 580. It should be noted that this linear range will be different for the coiled samples. Applicability of the Darcy permeability (Eq. (1)) was therefore tested, for each of our samples, by pressure-step testing during initial water flow-through (not shown). During these measurements, all four cement-filled steel tube samples showed laminar flow behaviour for the range of flow-rates employed in the (reactive) flow-through experiments. Behaviour corresponding with fully turbulent flow, estimated using the Blasius correlation, was observed in the capillary tube at Re > 2200 (Fig. A1).

References

Abdoulghafour, H., Luquot, L., Gouze, P., 2013. Characterization of the mechanisms controlling the permeability changes of fractured cements flowed through by CO2-rich brine. Environ. Sci. Technol. 47, 10332–10338, http://dx.doi.org/10.1021/es401317c.
Abdoulghafour, H., Gouze, P., Luquot, L., Leprovost, R., 2016. Characterization and modeling of the alteration of fractured class-G Portland cement during flow of CO2-rich brine. Int. J. Greenh. Gas Control., http://dx.doi.org/10.1016/j.ijggc.2016.01.032.
Al-Saiari, H.A., Yean, S., Tomson, M.B., Kan, A.T., 2008. Iron calcium carbonate: precipitation interaction. SPE International Oilfield Scale Conference. Society of Petroleum Engineers.
Andersson, K., Allard, B., Bengtsson, M., Magnusson, B., 1989. Chemical composition of cement pore solutions. Cem. Concr. Res. 19, 327–332, http://dx.doi.org/10.1016/0008-8846(89)90022-7.
Armitage, P.J., Faulkner, D.R., Worden, R.H., 2013. Caprock corrosion. Nat. Geosci. 6, 79–80.
Bachu, S., Bennion, D.B., 2009. Experimental assessment of brine and/or CO2 leakage through well cements at reservoir conditions. Int. J. Greenh. Gas Control 3, 494–501, http://dx.doi.org/10.1016/j.ijggc.2008.11.002.
Bachu, S., Watson, T., 2006. Possible indicators for CO2 leakage along wells. 8th International Conference on Greenhouse Gas Control Technologies, 19–22.
Barclay, I., Pellenbarg, J., Tettero, F., Pfeiffer, J., 2001. The beginning of the end: a review of abandonment and decommissioning practices. Oilf. Rev., 28–41.

Barlet-Gouédard, V., Rimmele, G., Porcherie, O., Quisel, N., Desroches, J., 2009. A solution against well cement degradation under CO2 geological storage environment. Int. J. Greenh. Gas Control 3, 206–216, http://dx.doi.org/10.1016/j.ijggc.2008.07.005.
Bear, J., 1972. Dynamics of Fluids in Porous Media. Dover Publications, Inc., New York.
Bernabe, Y., 1986. The effective pressure law for permeability in Chelmsford granite and Barre granite. Int. J. Rock Mech. Min. Sci. Geomech., 267–275, Abstract. Elsevier.
Bird, R.B., Stewart, W.E., Lightfoot, E.N., 2002. Transport Phenomena, 2nd ed. John Wiley & Sons, Inc., ISBN 0-471-41077-2.
Blasius, P.R.H., 1913. Das Ähnlichkeitsgesetz bei Reibungsvorgängen in Flüssigkeiten. Mitteilungen über Forschungsarbeiten auf dem Gebiete des Ingenieurwesens 131, 1–41.
Brown, G., 2002. The history of the Darcy-Weisbach equation for pipe flow resistance. In: Environmental and Water Resources History. American Society of Civil Engineers, pp. 34–43, http://dx.doi.org/10.1061/40650(2003)4.
Brunet, J.-P.L., Li, L., Karpyn, Z.T., Huerta, N.J., 2016. Fracture opening or self-sealing: critical residence time as a unifying parameter for cement–CO2–brine interactions. Int. J. Greenh. Gas Control 47, 25–37.
Cao, P., Karpyn, Z.T., Li, L., 2015. Self-healing of cement fractures under dynamic flow of CO2-rich brine. Water Resour. Res., http://dx.doi.org/10.1002/2014WR016162, n/a–n/a.
Carey, J.W., Wigand, M., Chipera, S.J., WoldeGabriel, G., Pawar, R., Lichtner, P.C., Wehner, S.C., Raines, M.A., Guthrie, G.D., 2007. Analysis and performance of oil well cement with 30 years of CO2 exposure from the SACROC Unit, West Texas, USA. Int. J. Greenh. Gas Control 1, 75–85, http://dx.doi.org/10.1016/S1750-5836(06)00004-1.
Carey, J.W., Svec, R., Grigg, R., Lichtner, P.C., Zhang, J., Crow, W., 2009. Wellbore integrity and CO2 –brine flow along the casing-cement microannulus. Energy Procedia 1, 3609–3615, http://dx.doi.org/10.1016/j.egypro.2009.02.156.
Carey, J.W., Svec, R., Grigg, R., Zhang, J., Crow, W., 2010. Experimental investigation of wellbore integrity and CO2–brine flow along the casing–cement microannulus. Int. J. Greenh. Gas Control 4, 272–282.
Carey, J.W., 2013. Geochemistry of wellbore integrity in CO2 sequestration: Portland cement-steel-brine-CO2 interactions. Rev. Mineral. Geochem. 77, 505–539.
Celata, G.P., Cumo, M., Guglielmi, M., Zummo, G., 2002. Experimental investigation of hydraulic and single-phase heat transfer in 0.130-mm capillary tube. Microscale Thermophys. Eng. 6, 85–97, http://dx.doi.org/10.1080/10893950252901240.
Celia, M.A., Nordbotten, J.M., Bachu, S., Dobossy, M., Court, B., 2009. Risk of leakage versus depth of injection in geological storage. Energy Procedia 1, 2573–2580, http://dx.doi.org/10.1016/j.egypro.2009.02.022.
Choi, Y.-S., Young, D., Nešić, S., Gray, L.G.S., 2013. Wellbore integrity and corrosion of carbon steel in CO2 geologic storage environments: a literature review. Int. J. Greenh. Gas Control 16, S70–S77.
Crow, W., Carey, J.W., Gasda, S., Brian Williams, D., Celia, M.A., 2010. Wellbore integrity analysis of a natural CO2 producer. Int. J. Greenh. Gas Control 4, 186–197, http://dx.doi.org/10.1016/j.ijggc.2009.10.010.
Deremble, L., Loizzo, M., Huet, B., Lecampion, B., Quesada, D., 2011. Stability of a leakage pathway in a cemented annulus. Energy Procedia 4, 5283–5290.
Dražić, D.M., Hao, C.S., 1982. The anodic dissolution process on active iron in alkaline solutions. Electrochim. Acta 27, 1409–1415.
Duan, Z., Sun, R., 2003. An improved model calculating CO2 solubility in pure water and aqueous NaCl solutions from 273 to 533 K and from 0 to 2000 bar. Chem. Geol. 193, 257–271.
Duguid, A., Scherer, G.W., 2010. Degradation of oilwell cement due to exposure to carbonated brine. Int. J. Greenh. Gas Control 4, 546–560, http://dx.doi.org/10.1016/j.ijggc.2009.11.001.
Duguid, A., Radonjic, M., Scherer, G.W., 2011. Degradation of cement at the reservoir/cement interface from exposure to carbonated brine. Int. J. Greenh. Gas Control 5, 1413–1428.
Duguid, A., 2009. An estimate of the time to degrade the cement sheath in a well exposed to carbonated brine. Energy Procedia 1, 3181–3188, http://dx.doi.org/10.1016/j.egypro.2009.02.101.
Dusseault, M.B., Gray, M.N., Nawrocki, P., 2000. Why oilwells leak: cement behavior and long-term consequences. SPE International Oil and Gas Conference and Exhibition, SPE 64733, http://dx.doi.org/10.2118/64733-MS, p. 8.
Engkvist, I., Albinsson, Y., Johansson Engkvist, W., 1996. The Long-term Stability of Cement: Leaching Tests. Swedish Nuclear Fuel and Waste Management Co.
Feia, S., Dupla, J.C., Ghabezloo, S., Sulem, J., Canou, J., Onaisi, A., Lescanne, H., Aubry, E., 2015. Experimental investigation of particle suspension injection and permeability impairment in porous media. Geomech. Energy Environ. 3, 24–39.
Fleury, M., Deschamps, H., 2008. Electrical conductivity and viscosity of aqueous NaCl solutions with dissolved CO2. J. Chem. Eng. Data 53, 2505–2509.
Gasda, S.E., Bachu, S., Celia, M.A., 2004. Spatial characterization of the location of potentially leaky wells penetrating a deep saline aquifer in a mature sedimentary basin. Environ. Geol. 46, 707–720, http://dx.doi.org/10.1007/s00254-004-1073-5.
Geloni, C., Giorgis, T., Battistelli, A., 2011. Modeling of rocks and cement alteration due to CO2 injection in an exploited gas reservoir. Transp. Porous Media 90, 183–200, http://dx.doi.org/10.1007/s11242-011-9714-0.
Guéguen, Y., Palciauskas, V., 1994. Introduction to the Physics of Rocks. Princeton University Press.

Hagen, G., 1839. Über die Bewegung des Wassers in engen cylindrischen Röhren. Ann. Phys. 122, 423–442.

Han, J., Carey, J.W., Zhang, J., 2011. A coupled electrochemical–geochemical model of corrosion for mild steel in high-pressure CO2–saline environments. Int. J. Greenh. Gas Control 5, 777–787.

Han, J., Carey, J.W., Zhang, J., 2012. Degradation of cement-steel composite at bonded steel-cement interfaces in supercritical CO2 saturated brines simulating wellbore systems. NACE – International Corrosion Conference Series, 151–179.

Hidalgo, A., Domingo, C., Garcia, C., Petit, S., Andrade, C., Alonso, C., 2008. Microstructural changes induced in Portland cement-based materials due to natural and supercritical carbonation. J. Mater. Sci. 43, 3101–3111.

Hofstee, C., Seeberger, F., Orlic, B., Mulders, F., Van Bergen, F., Bisschop, R., 2008. The feasibility of effective and safe carbon dioxide storage in the De Lier gas field. First Break 26, 53–57.

Hsieh, P.A., V, Bredehoeft, J.D., Silliman, S.E., 1981. A transient laboratory method for determining the hydraulic properties of tightrocks—I. Theory. Int. J. Rock Mech. Min. Sci. Geomech., 245–252, Abstract. Elsevier.

Huerta, N.J., Bryant, S.L., Strazisar, B.R., Kutchko, B.G., Conrad, L.C., 2009. The influence of confining stress and chemical alteration on conductive pathways within wellbore cement. Energy Procedia 1, 3571–3578, http://dx.doi.org/10.1016/j.egypro.2009.02.151.

Huerta, N.J., Bryant, S.L., Strazisar, B.R., Hesse, M., 2011. Dynamic alteration along a fractured cement/cement interface: implications for long term leakage risk along a well with an annulus defect. Energy Procedia 4, 5398–5405.

Huerta, N.J., Hesse, M.A., Bryant, S.L., Strazisar, B.R., Lopano, C., 2016. Reactive transport of CO2-saturated water in a cement fracture: application to wellbore leakage during geologic CO2 storage. Int. J. Greenh. Gas Control 44, 276–289, http://dx.doi.org/10.1016/j.ijggc.2015.02.006.

Ingraffea, A.R., Wells, M.T., Santoro, R.L., Shonkoff, S.B.C., 2014. Assessment and risk analysis of casing and cement impairment in oil and gas wells in Pennsylvania, 2000–2012. Proc. Natl. Acad. Sci. 111, 10955–10960, http://dx.doi.org/10.1073/pnas.1323422111.

Islam, A.W., Carlson, E.S., 2012. Viscosity models and effects of dissolved CO2. Energy Fuels 26, 5330–5336.

Jackson, R.E., Dusseault, M.B., 2014. Gas release mechanisms from energy wellbores. ARMA, 14–7753.

Jung, H.B., Kabilan, S., Carson, J.P., Kuprat, A.P., Um, W., Martin, P., Dahl, M., Kafentzis, T., Varga, T., Stephens, S., Arey, B., Carroll, K.C., Bonneville, A., Fernandez, C.A., 2014. Wellbore cement fracture evolution at the cement-basalt caprock interface during geologic carbon sequestration. Appl. Geochem. 47, 1–16, http://dx.doi.org/10.1016/j.apgeochem.2014.04.010.

Kampman, N., Burnside, N.M., Shipton, Z.K., Chapman, H.J., Nicholl, J.A., Ellam, R.M., Bickle, M.J., 2012. Pulses of carbon dioxide emissions from intracrustal faults following climatic warming. Nat. Geosci. 5, 352–358.

Kutchko, B.G., Strazisar, B.R., Dzombak, D.A., Lowry, G.V., Thaulow, N., 2007. Degradation of well cement by CO2 under geologic sequestration conditions. Environ. Sci. Technol. 41, 4787–4792.

Kutchko, B.G., Strazisar, B.R., Lowry, G.V., Dzombak, D.A., Thaulow, N., 2008. Rate of CO2 attack on hydrated Class H well cement under geologic sequestration conditions. Environ. Sci. Technol. 42, 6237–6242.

Kutchko, B.G., Strazisar, B.R., Huerta, N., Lowry, G.V., Dzombak, D.A., Thaulow, N., 2009. CO2 reaction with hydrated class H well cement under geologic sequestration conditions: effects of flyash admixtures. Environ. Sci. Technol. 43, 3947–3952, http://dx.doi.org/10.1021/es803007e.

Lecampion, B., Quesada, D., Loizzo, M., Bunger, A., Kear, J., Deremble, L., Desroches, J., 2011. Interface debonding as a controlling mechanism for loss of well integrity: importance for CO2 injector wells. Energy Procedia 4, 5219–5226, http://dx.doi.org/10.1016/j.egypro.2011.02.500.

Lecampion, B., Bunger, A., Kear, J., Quesada, D., 2013. Interface debonding driven by fluid injection in a cased and cemented wellbore: modeling and experiments. Int. J. Greenh. Gas Control 18, 208–223, http://dx.doi.org/10.1016/j.ijggc.2013.07.012.

Liteanu, E., Spiers, C.J., 2011. Fracture healing and transport properties of wellbore cement in the presence of supercritical CO2. Chem. Geol. 281, 195–210, http://dx.doi.org/10.1016/j.chemgeo.2010.12.008.

Lothenbach, B., Winnefeld, F., Alder, C., Wieland, E., Lunk, P., 2007. Effect of temperature on the pore solution, microstructure and hydration products of Portland cement pastes. Cem. Concr. Res. 37, 483–491.

Lothenbach, B., Matschei, T., Möschner, G., Glasser, F.P., 2008. Thermodynamic modelling of the effect of temperature on the hydration and porosity of Portland cement. Cem. Concr. Res. 38, 1–18.

Luquot, L., Abdoulghafour, H., Gouze, P., 2013. Hydro-dynamically controlled alteration of fractured Portland cements flowed by CO2-rich brine. Int. J. Greenh. Gas Control 16, 167–179, http://dx.doi.org/10.1016/j.ijggc.2013.04.002.

Mainguy, M., Longuemare, P., Audibert, A., Lécolier, E., 2007. Analyzing the risk of well plug failure after abandonment. Oil Gas Sci. Technol. Rev. 62, 311–324, http://dx.doi.org/10.2516/ogst.

Mao, S., Duan, Z., 2009. The viscosity of aqueous alkali-chloride solutions up to 623 K, 1000 bar, and high ionic strength. Int. J. Thermophys. 30, 1510–1523, http://dx.doi.org/10.1007/s10765-009-0646-7.

Mason, H.E., Du Frane, W.L., Walsh, S.D.C., Dai, Z., Charnvanichborikarn, S., Carroll, S.A., 2013. Chemical and mechanical properties of wellbore cement altered by CO$_2$-rich brine using a multianalytical approach. Environ. Sci. Technol. 47, 1745–1752, http://dx.doi.org/10.1021/es3039906.

Matschei, T., Glasser, F.P., 2007. Interactions between Portland cement and carbon dioxide. In: Proc. 12th ICCC, Montr.

Montgomery, C.T., 2006. Implications of cementing for well production and performance. In: Nelson, E.B., Guillot, D. (Eds.), Well Cementing. Schlumberger, Sugar Land, TX 77478, USA, p. 773.

Nešić, S., 2007. Key issues related to modelling of internal corrosion of oil and gas pipelines – a review. Corros. Sci. 49, 4308–4338.

Neuzil, C.E., Cooley, C., Silliman, S.E., Bredehoeft, J.D., Hsieh, P.A., 1981. A transient laboratory method for determining the hydraulic properties of tightrocks—II. Application. Int. J. Rock Mech. Min. Sci. Geomech., 253–258, Abstract. Elsevier.

Newell, D.L., Carey, J.W., 2012. Experimental evaluation of wellbore integrity along the cement-rock boundary. Environ. Sci. Technol. 47, 276–282.

Nogues, J.P., Fitts, J.P., Celia, M.A., Peters, C.A., 2013. Permeability evolution due to dissolution and precipitation of carbonates using reactive transport modeling in pore networks. Water Resour. Res. 49, 6006–6021, http://dx.doi.org/10.1002/wrcr.20486.

Orlic, B., 2009. Some geomechanical aspects of geological CO2 sequestration. KSCE J. Civ. Eng. 13, 225–232, http://dx.doi.org/10.1007/s12205-009-0225-2.

Papaevangelou, G., Evangelides, C., Tzimopoulos, C., 2010. A new explicit relation for the friction coefficient in the Darcy-Weisbach equation. Proceedings of the Tenth Conference on Protection and Restoration of the Environment, 6–9.

Poiseuille, J.L., 1844. Recherches expérimentales sur le mouvement des liquides dans les tubes de très-petits diamètres. Imprimerie Royale.

Raoof, A., Nick, H.M., Wolterbeek, T.K.T., Spiers, C.J., 2012. Pore-scale modeling of reactive transport in wellbore cement under CO2 storage conditions. Int. J. Greenh. Gas Control 11, S67–S77, http://dx.doi.org/10.1016/j.ijggc.2012.09.012.

Rimmelé, G., Barlet-Gouédard, V., Porcherie, O., Goffé, B., Brunet, F., 2008. Heterogeneous porosity distribution in Portland cement exposed to CO2-rich fluids. Cem. Concr. Res. 38, 1038–1048, http://dx.doi.org/10.1016/j.cemconres.2008.03.022.

Rothstein, D., Thomas, J.J., Christensen, B.J., Jennings, H.M., 2002. Solubility behavior of Ca-, S-, Al-, and Si-bearing solid phases in Portland cement pore solutions as a function of hydration time. Cem. Concr. Res. 32, 1663–1671, http://dx.doi.org/10.1016/S0008-8846(02)00855-4.

Rutqvist, J., 2012. The geomechanics of CO2 storage in deep sedimentary formations. Geotech. Geol. Eng. 30, 525–551.

Sutera, S.P., Skalak, R., 1993. The history of Poiseuille's law. Annu. Rev. Fluid Mech. 25, 1–20.

Taylor, H.F.W., 1992. Cement Chemistry. Academic Press Limited, London, UK.

Taylor, J.R., 1997. Introduction to Error Analysis, the Study of Uncertainties in Physical Measurements, 2nd ed. University Science Books, ISBN 0-935702-75-X.

ter Heege, J.H., Orlic, B., Hoedeman, G.C., 2015. Characteristics of mechanical wellbore failure and damage: insights of discrete element modelling and application to CO2 storage. ARMA, 15–174.

Trinh, K.T., 2010. On the Blasius correlation for friction factors. arXiv Prepr. arXiv1007.2466.

Villain, G., Thiery, M., Platret, G., 2007. Measurement methods of carbonation profiles in concrete: thermogravimetry, chemical analysis and gammadensimetry. Cem. Concr. Res. 37, 1182–1192.

Walsh, S.D.C., Mason, H.E., Du Frane, W.L., Carroll, S.A., 2014a. Experimental calibration of a numerical model describing the alteration of cement/caprock interfaces by carbonated brine. Int. J. Greenh. Gas Control 22, 176–188, http://dx.doi.org/10.1016/j.ijggc.2014.01.004.

Walsh, S.D.C., Mason, H.E., Du Frane, W.L., Carroll, S.A., 2014b. Mechanical and hydraulic coupling in cement-caprock interfaces exposed to carbonated brine. Int. J. Greenh. Gas Control 25, 109–120, http://dx.doi.org/10.1016/j.ijggc.2014.04.001.

Whittaker, S., Rostron, B., Hawkes, C., Gardner, C., White, D., Johnson, J., Chalaturnyk, R., Seeburger, D., 2011. A decade of CO2 injection into depleting oil fields: monitoring and research activities of the IEA GHG Weyburn-Midale CO2 Monitoring and Storage Project. Energy Procedia 4, 6069–6076, http://dx.doi.org/10.1016/j.egypro.2011.02.612.

Wigand, M., Kaszuba, J.P., Carey, J.W., Hollis, W.K., 2009. Geochemical effects of CO2 sequestration on fractured wellbore cement at the cement/caprock interface. Chem. Geol. 265, 122–133, http://dx.doi.org/10.1016/j.chemgeo.2009.04.008.

Wolterbeek, T.K.T., Peach, C.J., Spiers, C.J., 2013. Reaction and transport in wellbore interfaces under CO2 storage conditions: experiments simulating debonded cement-casing interfaces. Int. J. Greenh. Gas Control 19, 519–529, http://dx.doi.org/10.1016/j.ijggc.2013.10.017.

Wolterbeek, T.K.T., Hangx, S.J.T., Spiers, C.J., 2016. Effect of CO2-induced reactions on the mechanical behaviour of fractured wellbore cement. Geomech. Energy Environ. 7, 26–46.

Yalcinkaya, T., Radonjic, M., Willson, C.S., Bachu, S., 2011. Experimental study on a single cement-fracture using CO2 rich brine. Energy Procedia 4, 5335–5342, http://dx.doi.org/10.1016/j.egypro.2011.02.515.

Zhang, M., Bachu, S., 2011. Review of integrity of existing wells in relation to CO2 geological storage: what do we know? Int. J. Greenh. Gas Control 5, 826–840, http://dx.doi.org/10.1016/j.ijggc.2010.11.006.

Zwanzig, R., Harrison, A.K., 1985. Modifications of the Stokes–Einstein formula. J. Chem. Phys. 83.